Swarms and mainshock-aftershocks sequences are both triggered by fluids in the Ubaye Region (Western Alps)

Marion Baques, Louis de Barros, Maxime Godano, Clara Duverger, Hervé Jomard

Swarms and mainshock-aftershocks sequences are both triggered by fluids in the Ubaye Region (Western Alps).

Marion Baques [1], Louis De Barros [1], Maxime Godano [1], Clara Duverger [2] and Hervé Jomard [3]

1: Université Côte d'Azur, CNRS, Observatoire de la Côte d'Azur, IRD, Géoazur, 250 rue Albert Einstein, Sophia Antipolis 06560 Valbonne, France

2: CEA, DAM, DIF, F-91297 Arpajon, France

3: Bureau d'évaluation des risques sismiques pour la sûreté des installations, Institut de Radioprotection et Sûreté Nucléaire, Fontenay-aux-Roses, France

Abbreviated title:

Fluid-triggered mainshock-aftershocks and swarms

Corresponding author: Baques Marion Mail: marion.baques@geoazur.unice.fr

Abstract

The Ubaye Region (French Western Alps) is one of the most seismically active regions in France. It is regularly struck by mainshock-aftershocks sequences like in 1959 (ML5.3), seismic swarms (2003-2004), and complex sequences (2012-2015) characterized by successive mainshocks clustered in time and space. This diversity of seismic behaviour highlights the complex processes at play in this area. To improve our understanding of these processes, in this study, we compile a regional catalogue of existing focal mechanisms, completed by 100 new calculated focal mechanisms of aftershocks following the 07/04/2014 mainshock (ML5.1). The oriented stress-state we reconstruct for different periods and sub-areas are similar to each other and to previous published values focusing on swarm periods. We then calculate fluid-pressure required to trigger the earthquakes. Most of the events (65%) need fluid-overpressure between 15 and 40 MPa (17-to-40% of the hydrostatic pressure) with a median value of 24%. Moreover, even the largest events, like the mainshocks in the 2012-2015 sequence, appear to be triggered by fluid-pressure, similarly as events within swarm sequences. However, while fluid-overpressure decreases with time in an aftershock sequence, it varies randomly at high levels during a swarm sequence. Therefore, based on a fault-valve model, we propose that: 1) the fluids trapped in the fault plane tend toward lithostatic pressure and trigger the mainshock rupture and 2) part of the aftershocks are induced by the diffusing fluid-pressure. On the contrary, swarms need external, likely deep, fluid-pressure feedings. Fluid-pressure is likely to be a common triggering mechanism of the seismicity in the Ubaye Region, even if the involved processes should differ to explain the different types of seismic sequences.

Keywords

Europe; Earthquake dynamics; Seismicity and tectonics; Dynamics and mechanisms of faulting; Fluid-driven seismicity

1. Introduction

Two end-member behaviours may characterize earthquake sequences: mainshock-aftershocks sequences and swarm sequences. On one hand, mainshock-aftershocks sequence is the most common behaviour and starts with the largest magnitude earthquake, possibly damaging, followed by aftershocks of lower magnitude. Aftershocks are mainly driven by coseismic stress transfer (Stein, 1999) and occur around the fault zone where the mainshock occurred. However, some of the aftershocks sequences may also have been triggered by fluid-pressure, reactivating fault by high fluid-pressure (e.g. Gunatilake, 2023). The number of aftershocks decays with time following an Omori-Utsu's law (Utsu and Ogata, 1995). Such mainshock-aftershocks sequences occur in all tectonically active contexts, as the tectonic stress loading directly triggers them. On the other hand, swarm sequences are bursts of earthquakes, usually of small-to-moderate magnitudes, which are clustered in time and space. They are characterized by a slow increase and decrease of the seismicity rate without a clear pattern, and by the strongest event occurring at any time during the sequence. They also occur in different tectonic settings: subduction zones (e.g. Japan, Kato *et al.* 2014; Nishikawa and Ide, 2017), volcanic regions (e.g. Mayotte, Bertil *et al.* 2021) or stable intraplate areas (e.g. Western Bohemia, Fischer et *al.* 2014). They can last for days (e.g. Mammoth Mountain, Shelly and Hill, 2011; Mount Rainier, Shelly *et al.* 2013; Corinth Gulf, De Barros *et al.* 2020; South Korea, Son *et al*. 2021) to years (e.g. Ubaye, Jenatton *et al*. 2007; Cahuilla swarm, Ross and Cochran, 2021; Japan, Amezawa *et al.* 2021). To maintain this activity, a driving mechanism that lasts in time is required. As swarms can also be induced by geothermal activities (e.g. Baisch et al., 2015; Schoenball et al., 2014) or hydrocarbon ressources exploitations (e.g. Goebel *et al.* 2016; Schultz *et al.* 2020) or even triggered by rainfalls during monsoon period (e.g. Gunatilake et al., 2021), they are commonly

69 associated with fluid-pressure diffusion at depth (e.g. Miller *et al.* 2004; Parotidis and Shapiro, 2004;
70 Terakawa *et al.* 2010). Classically, seismic failures are seen to be induced directly by the decrease of
71 normal effective stress associated with the increase of fluid-pressure. Seismic migration is then
72 explained by the fluid-pressure diffusion. Alternatively, swarm sequences were also observed to be
73 driven by slow-slips or aseismic deformation (Lohman and McGuire, 2007; Vallée *et al.* 2013). Fluid
74 and aseismic processes may also be imbricated to drive swarms as the first one drives the latter, as
75 observed in different contexts (Corinth Gulf, De Barros *et al.* 2020; Canada, Eyre *et al.* 2020) or
76 numerical simulations (e.g. Wynants-Morel *et al.* 2020). As no direct observations are possible in the
77 source area, swarm processes are still an open question.
78 In between these two end-member categories, more complex sequences exist. For example, some
79 sequences involve several cascading mainshocks, with a global swarm pattern (Colfiorito sequence,
80 Chiaraluce et *al.* 2003; Ubaye region, Thouvenot et *al.* 2016; Western Bohemia, Hainzl et *al.* 2016,
81 Jakoubková et *al.* 2018; Corinth Gulf, Kaviris et *al.* 2021). In the Ubaye Region (De Barros *et al.* 2019)
82 as well as in the Puerto Rico area (Ventura-Valentin and Brudzinski, 2021) or the Corinth Gulf (Kaviris
83 *et al.* 2021), authors observe that a mainshock started a seismic crisis, but with an abnormal number
84 of aftershocks that did not decay according to the expected Omori-Utsu's law and contained small
85 swarm sequences. In such cases, complex processes involving tectonic stress release as well as fluids
86 and/or aseismic-slip are required. The Amatrice-Visso-Norcia sequence (Appenines, Italy) was also a
87 complex seismic sequence during which the generation of internal fluids by decarbonisation seems
88 to be responsible for non-Omori type aftershock behaviour (Gunatilake and Miller, 2022).
89
90 The Ubaye Region, located in the Southwestern Alps, is one of the most seismically active area in
91 France. Mainshock-aftershocks, seismic swarms, and complex sequences have been observed since
92 the 18th century (Baques *et al.* 2021). In 2003-2004, more than 16,000 events were recorded in a
93 swarm sequence (Jenatton *et al.* 2007; Daniel *et al.* 2011; Leclère *et al.* 2013). The last seismic crisis
94 happened in 2012-2015 with two moderate earthquakes of magnitude ML4.8 and ML5.1, which

95 occurred at a similar location on 26/02/2012 and 07/04/2014, respectively. They were followed by
96 an abnormally high rate of seismicity (Thouvenot *et al.* 2016; De Barros *et al.* 2019), including several
97 small swarms at close distances from the mainshocks. Globally, this seismic crisis can be described as
98 a swarm, because the size of the seismic cluster is much larger than the spatial extent of the main
99 ruptures. As 1) the tectonic deformation is very limited in the Southern Alps (e.g. Mathey *et al.*
100 2021b; Walpersdorf *et al.* 2018), and 2) the areas just South or North of the Ubaye Valley are less
101 active seismically, complex processes are required to explain both the high rate of seismicity and its
102 complex patterns. For both the 2003-2004 swarm and the 2012-2015 sequence, fluid processes have
103 been raised (e.g. Leclère *et al.* 2013; Thouvenot *et al.* 2016; De Barros *et al.* 2019). For example,
104 seismic migration with a diffusivity of 0.002 to 0.06 m^2/s were observed for the 2003-2004 and
105 within the 2012-2015 sequences (Thouvenot *et al.* 2016; De Barros *et al.* 2019). These values are
106 similar to the measured ones for fluid-induced seismicity in reservoir exploitations (Shapiro *et al.*
107 2002) and for other swarms worldwide (Talwani *et al.* 2007). Leclère et *al.* (2013) proposed that
108 creep compaction pressurized the fluid within the fault, which then drove the 2003-2004 swarm
109 migration. Daniel et *al.* (2011) also proposed that fluid process is required, because stress-transfer
110 through earthquake-earthquake interaction explains only 59% of the 2003-2004 swarm. De Barros et
111 *al.* (2019) suggested an interplay between stress-transfer and fluid-driven process since only some
112 clusters in the 2014 aftershocks followed a typical aftershocks pattern, while others clearly behaved
113 as seismic swarms.
114
115 In this study, we aim at better understanding the processes at play, focusing both on the 2014
116 aftershocks period that was recorded by a dense temporary network (e.g. Baques *et al.*, 2021) and on
117 specific seismic sequences, such as the 2003-2004 seismic swarm and the 2012-2015 seismic crisis, to
118 explain the peculiar seismic behaviour in the Ubaye Region.
119

Direct observations of fluid are not possible at crustal depth. However, as fluid-pressure induces failures through reduction of the effective stress, it may trigger seismicity on fault planes that are misoriented with respect to the tectonic stress-state (Sibson, 1990). We therefore aim to compare the orientation of the observed failures, obtained through focal mechanisms, with the average stress-state. Using Cauchy's equations, we can reconstruct the fluid-pressure that is required within the faults to induce earthquakes. A similar approach was used by Leclère et *al.* (2013), but focusing only on the 2003-2004 swarm period. They showed that the seismicity required from 20 to 50 MPa of overpressure with ~35 MPa at the beginning of the swarm and increasing up to ~55 MPa during the peak of activity.

After presenting the general seismo-tectonic context of the area, we first describe the different focal mechanisms catalogues we use for the Ubaye Region, including the well-instrumented two-month period after the 2014 mainshock. We then present the methods used to reconstruct the stress-state and the fluid-pressure needed to trigger the seismicity. We apply these methods on the Ubaye Region and refine the results looking at sub-areas, for different time periods, and for the 2014 aftershocks. Finally, we propose and discuss a conceptual model that explains the role of fluid-driven process in the Ubaye Valley area.

2. Seismo-tectonic context

2.1. Tectonic context

The Alpine chain is divided into two zones, internal and external, delimited by the Frontal Penninic Thrust (FPT, Fig. 1). East of the FPT, in the intern zone, the Ubaye Region is mainly composed of the

Briançonnais unit, which consists of a pile of thick low grade metamorphic nappes (e.g. Sue *et al.* 2007). West of the FPT, the Dauphinois units is composed of a 1-to-2-km thick Mesozoic to Cenozoic sedimentary rock cover (sandstone, marls, and limestone, Kerckhove *et al.* 1978) laying on the crystalline basement (granitoid; Baietto *et al.,* 2009). Overlaying some parts of the Dauphinois units is the 1-to-2 km thick "Flysch à Helminthoïdes". This cover is also called the Embrunais-Ubaye nappes (Kerckhove, 1969) and is composed of late Cretaceous turbiditic series that were thrust westward during the Oligocene period (e.g. Gratier *et al.* 1989).

Crossing perpendicularly the Alpine structures, the Ubaye Valley gives us a view of the long geological history of compression and extension resulting from the setting of the Western Alps. The late Alpine faults as defined by Kerckhove (1969) and Tricart (2004) are the more recently recorded deformations. It consists in a series of normal and right lateral strike-slip faults formed or reactivated during the last Mio-Pliocene setting of the chain, and showing field evidence of neotectonic activity (Sue, 1998; Sue *et al.* 2007). Current seismicity seems to develop along them (Jenatton *et al.* 2007; Sue *et al.* 2007; Le Goff *et al.* 2009; Sanchez *et al.* 2010; Mathey *et al.* 2020; Fig. 1). A majority of these faults are oriented N-S to NW-SE with some minor conjugate structures oriented E-W to NE-SW (Kerckhove, 1969; Sue and Tricart, 2003; Tricart and Schwartz, 2006). The main identified active faults in the Ubaye Region are the High-Durance, the Serenne, and the Jausiers-Tinée faults (Fig. 1; Baques et *al.* 2021; Mathey et *al.* 2020). The first is oriented N-S and is prolonged to the Southeast by the Serenne fault. These two faults are located east of the Frontal Penninic Thrust while the Jausiers-Tinée fault (external part) is parallel to and at about 10 km south of the Serenne fault.

Using satellite geodesy, there is no measurable horizontal strain (e.g. Walpersdorf et *al.* 2018). For the vertical deformation, Mathey et *al.* (2021b) used INSAR data to obtain the vertical strain-rate in the Western Alps and found a range of ~-0.7mm/yr to ~0.5mm/yr for the Ubaye Region (see Fig. 3 in Mathey et *al.* 2021b). Therefore, vertical deformation is very limited and not homogenous in the Ubaye Region.

168 Several studies computed earthquake focal mechanisms and calculated stress-state in the Ubaye
169 Region and its surrounding areas to determine the tectonic stress regime. The mechanisms showed a
170 dominant extensional regime with a strike-slip component for the Ubaye Region (Fig. 1). Mathey et
171 *al.* (2021b) found that the extensional component is oblique to the strike of the Alpine belt, while it
172 was assumed normal until now (Sue *et al.* 2007). Similar stress-states have been reconstructed for
173 the last swarms (2003-2004 and 2012-2015) occurring in the Ubaye Region (Leclère *et al.* 2013;
174 Fojtíková and Vavryčuk, 2018).

175

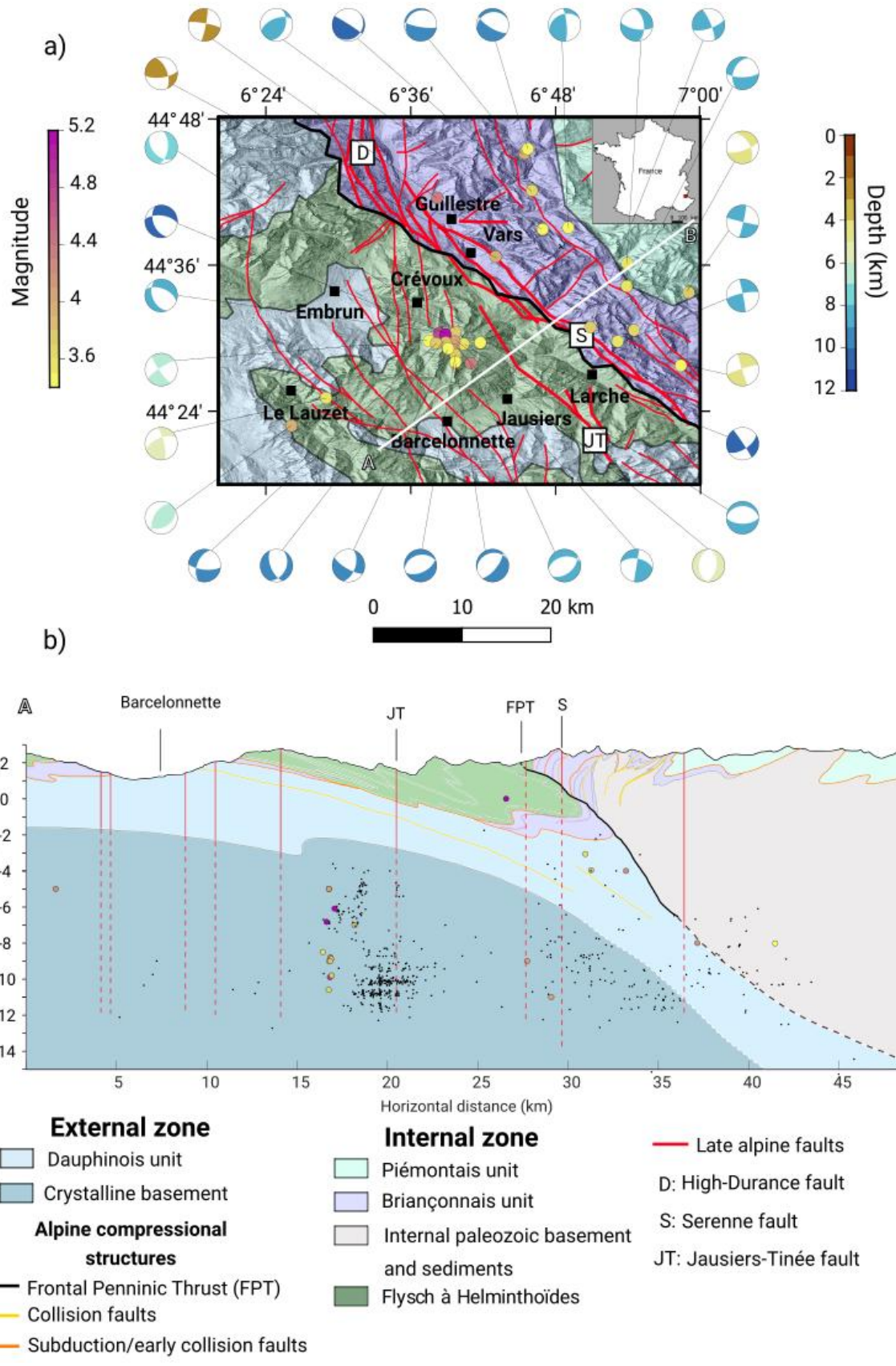

Figure 1: a) Simplified geological map of the Ubaye Region with focus on the late Alpine faults. (red lines, from Tricart, 2004). Dots correspond to the location of earthquakes with their local magnitude

ML (from the LDG, Duverger *et al*. (2021)) greater than 3.2, the colour being proportional to ML. Focal mechanisms of the largest events are from several catalogues: Fréchet and Pavoni (1979), Leclère *et al*. (2013), Thouvenot *et al*. (2016), FMHex20 (Mazzotti *et al.* 2021) and Mathey *et al*. (2021a). Their colours show the depth of the events. The clusters of events between Crévoux, Jausiers, and Barcelonnette (2003-2004 and 2012-2015 swarms) have been artificially dispersed for better visualization. b), Simplified geological cross-section oriented N050°, modified from Dumont *et al.* (2022). The dots show the events with a computed focal mechanism (Fig. 2b). Black dots are events with magnitude smaller than 3.2, while larger magnitude are coloured according to the scale in a).. Only the events contained in a buffer of 10km apart from the cross-sections are represented. The late Alpine faults are extended at depth by dotted lines for illustration but no information on the

dip of the faults at depth is available

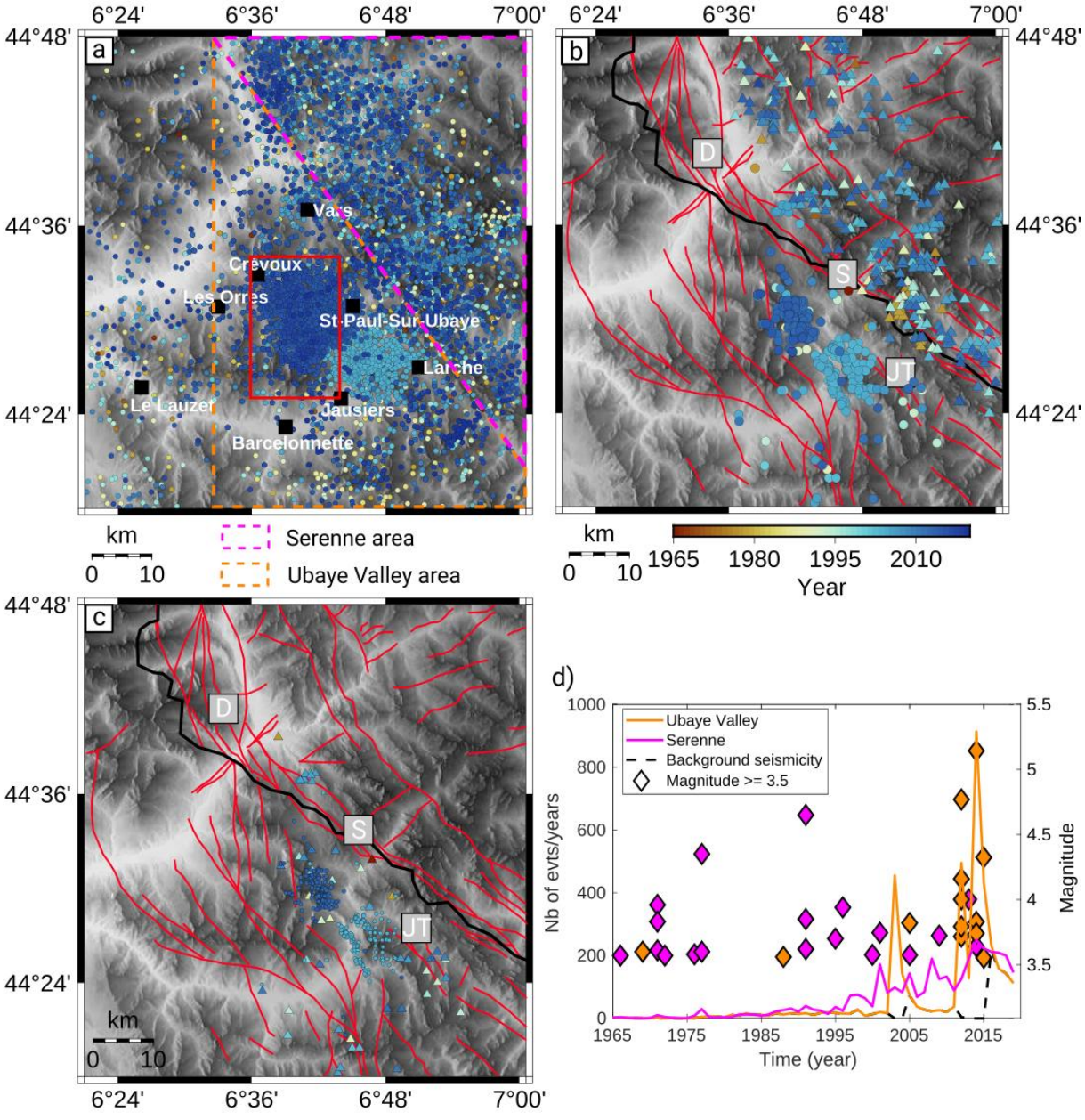

Figure 2: a) Map of the instrumental seismicity since 1965 (LDG catalogue, http://www-dase.cea.fr). The orange and pink dashed-line zones delimit the Ubaye Valley and the Serenne area respectively, and the red square shows the 2014 relocated aftershock area (Fig. 3). b) Map of the earthquakes with a computed focal mechanism in the Ubaye Valley (circle) and the Serenne area (triangle) coloured by the year of occurrence. c) Map of the earthquakes with computed focal mechanisms for the 2003-2004 swarms (light blue circle), the 2012-2015 sequence (dark blue circle), and of the background seismicity (triangle) coloured by the year of occurrence. In b) and c), the red lines

correspond to the late Alpine faults mapped by Tricart (2004): D = High-Durance fault; S = Serenne fault; JT = Jausiers-Tinée fault. d) Distribution of earthquakes in the LDG catalogue as function of the time (years) for two different areas: the Ubaye Valley (orange) and the Serenne area (purple). The dashed black line (Background seismicity) corresponds to events that occurred in the Ubaye Valley during the periods: 1965-2002, 2005-2011, and 2016-2020. The diamonds correspond to the events with magnitude greater than or equal to 3.5.

2.2. Seismic activity

Even if background seismicity is scattered in the full area, most events are located in two main areas: in a large band along the Serenne and High-Durance faults in the internal units later referred as "Serenne area", and in large clusters between Crévoux, St-Paul-sur-Ubaye, and Barcelonnette in the external units later referred as "Ubaye Valley area" (Fig. 2). The seismicity in these two areas behaves differently (Baques *et al.* 2021; Larroque *et al.* 2021). In the Ubaye Valley, the seismicity mainly occurs in clusters (Fig. 2a) and shows both mainshock-aftershocks and swarm sequences. On the contrary, in the Serenne area, the seismicity is more scattered without clear clustered zones. The seismicity mainly develops as mainshock-aftershocks sequences. Yet, the presence of small seismic swarms cannot be discarded as no specific studies have been made on this area. In the following, we briefly describe the two clusters that occurred in 2003-2004 and 2012-2015 in the Ubaye Valley area.

The 2003-2004 swarm (Fig. 2, light blue circles) started in early 2003 with seismic activity slowly increasing until July 2003. The seismicity rate remained at a high level for 3 months with the strongest earthquakes (maximum magnitude of ML_{LDG}3.4) occurring during the end of the summer 2003. Then the seismicity rate slowly decreased to reach the background seismicity rate in the summer 2004 (Jenatton *et al.* 2007; Baques *et al.* 2021). Finally, a small burst of activity occurred at the end of 2004. More than 16,000 earthquakes were detected between 3km and 8km depth

(crystalline basement) and aligned along a 9km long structure oriented N150°E. Leclère et *al.* (2013) computed 74 focal mechanisms that showed combined right lateral strike-slip motions along N150°-to-N175°E structures with extensional components. Among the focal mechanisms, one of their nodal planes shows similar orientation as the main direction of the cluster (~N150°E, Jenatton et *al.* 2007) and to the orientation of the Jausiers-Tinée fault system. Leclère et *al.* (2013) proposed that the Embrunais-Ubaye nappes, as well as the thick Mesozoic marly layers play the role of cap rock, allowing the fluids to pressurize the upper crust and generate earthquake swarms.

Ten years later, the 2012-2015 sequence started 7 km north-west of the 2003-2004 swarm, (Fig. 2, dark blue circles) on 26 February 2012 with a ML_{LDG}4.8 (Mw4.2) earthquake at 8.8 km depth. It was followed two years later, on 7 April 2014, by a larger shock of ML_{LDG}5.2 (Mw4.8), which occurred exactly at the same location but slightly deeper (9.9 km, Thouvenot et *al.* 2016). These mainshocks were felt in Nice and Grenoble, 100 km from the epicentre area (Sira *et al.* 2012, 2014; Courboulex *et al.* 2013). Following the two mainshocks, intense seismic crises started, and the 2014 crisis instantaneously reactivated the 2012 crisis area. The seismicity then globally decreased as aftershock sequences (Thouvenot *et al.* 2016; De Barros *et al.* 2019). During the two months (10 April 2014 - 10 June 2014) following the 7 April 2014 mainshock, a temporary network of 7 seismic stations was deployed at 5 to 16 km from the mainshock epicentre. More than 9,000 events were detected by template-matching and ~6,000 of them were relocated (Fig. 3) using a double-difference relocation by De Barros et *al.* (2019). A modified Omori-Utsu's law (Utsu, 1961) fitted on these events showed a p=0.77 time exponent, which is slower than usual and reflects a more complex behaviour (see Fig. 5 in De Barros *et al.*, 2019). This aftershock sequence is interpreted as composed of intertwined aftershock-like clusters and swarm sequences (De Barros *et al.* 2019). After the 2014 mainshock-aftershocks sequence, an event of ML_{LDG}3.6 (Mw=3.4) occurred in mid-April 2015, followed by another of ML_{LDG}4.3 (Mw=4.2) in November 2015. Despite some classical mainshock-aftershocks

sequence characteristics, the full crisis (2012-2015) follows a swarm-like behaviour with the largest event in the middle of the temporal sequence and a spatial extension much larger than the rupture dimension of the largest event. The majority of the seismicity occurred in the crystalline basement between 4 km and 10 km depth and aligned along a N160°E major structure and some N50°E minor structures (Fig. 3, Fig. S1). These orientations are retrieved in the 13 focal mechanisms computed by Thouvenot et *al.* (2016). In addition, no seismicity occurred in the area between the 2003-2004 swarm and the 2012-2015 sequence (Thouvenot *et al.* 2016). The activated structures, well illuminated at depth (Thouvenot *et al.* 2016; De Barros *et al.* 2019) are not identified in the surface geology, possibly due to the compliant sedimentary materials, which make it difficult to locate and recognize active deformation. On the contrary, active structures are identified at the surface in the internal zone (Sue *et al.* 2007), but the diffuse nature of seismicity does not allow to clearly associate the seismicity to well identified single fault systems.

3. Data: focal mechanisms

In this study, we based our analysis on existing focal mechanisms computed previously in the Ubaye Region, and on focal mechanisms specially computed for the two months aftershocks following the 7 April 2014 mainshock.

3.1 Ubaye Region

Thereafter, we gathered all the available focal mechanisms in a catalogue (full Ubaye Region catalogue). This catalogue is composed of the FMHex20 catalogue from Mazzotti et *al.* (2021), mechanisms from Fréchet and Pavoni (1979), Leclère et *al.* (2013), Thouvenot et *al.* (2016), and

Mathey et *al.* (2021a). In total, 799 focal mechanisms composed the full Ubaye Region catalogue, those with a magnitude larger than ML_{LDG}3.4 (4% of the events) are displayed in Fig. 1. About 39% of the focal mechanisms occurred with a pure strike-slip to strike-slip motion with a normal component, while ~40% of the events show a pure normal to normal with a strike-slip component mechanism (Fig. S2, Tab. S1). The remaining part shows strike-slip with a reverse component (12%) or reverse mechanism (~9%). Two orientations stand out: N145°-to-N250°, N330°-to-N65° (Fig. S3). These orientations are compatible with the active faults in the area. Indeed, the N145°-to-N250° is similar to the orientation of the Serenne fault (N150°), while the N330°-to-N65°direction is consistent with the High-Durance fault and with conjugate faults of the Serenne fault (Fig. 1).

We then refine the full catalogue by separating mechanisms from the Ubaye Valley (453 events, Fig. 2b) and from the Serenne area (314 events, Fig. 2b). We also create two subsets of focal mechanisms for the Ubaye Valley: the 2003-2004 swarm area (138 events, Fig. 2c) and the 2012-2015 sequence area (260 events, Fig. 2c). The remaining focal mechanisms in the Ubaye Valley are gathered to form a background seismicity catalogue (55 events, Fig. 2c) that covers the periods of 1965-2002, 2005-2011, and 2016-2020. No significant differences are observed either in the distributions of the fault mechanisms or in the nodal plane orientations among the different sub-catalogues (see Tab.S1 and Fig. S2).

3.2 2014 Aftershocks

For this sequence, only 3 focal mechanisms were already computed (Thouvenot *et al.* 2016; Mathey *et al.* 2021a). We choose to refine the analysis by computing the focal mechanisms of the largest events in the relocated catalogue of De Barros et al., 2019. In total, 15 seismic stations were used: 7 from the temporary network and 8 permanent ones (3 from the INGV network (University of Genoa., 1967; INGV Seismological Data Centre, 2006); 5 from the RESIF network (RESIF, 1995)). For each

294 event, we invert simultaneously the P-wave polarity and the S-to-P-waves amplitude ratio to
295 determine the focal mechanisms (Godano (2009), Godano et *al.* (2014)). For the amplitude ratio, we
296 first picked the amplitude of the first arrival for the P- and S-waves on the three components and
297 calculated the norm for both wave types. We carefully check the consistency of our results with the
298 focal mechanisms obtained by Thouvenot et *al.* (2016). Examples of focal mechanisms and their
299 uncertainties, together with the P-wave polarities and the S/P amplitude ratio, are shown in
300 Supplementary Fig. S4. We computed the mechanisms for which polarity and amplitude ratio are
301 available from at least 7 stations. At the end of the inversion, we kept solutions for which inversion
302 leads to score (inversed misfit function) greater than 0.4 (see Godano et al. 2014). The 100 focal
303 mechanisms then form the 2014 relocated aftershocks catalogue.

304 The 2014 relocated aftershocks catalogue is mainly composed of 70% of pure-normal to normal
305 mechanisms with a strike-slip component and 20% of strike-slip mechanisms with a normal
306 component (Tab.S1 and Fig. S2). Even if the ratio of normal mechanisms is higher than in the Ubaye
307 Valley catalogue (Fig. S2), we retrieve similar orientations for the nodal planes (N170°-to-N230°,
308 N355°-to-N70°; Fig. S3). However, we do not retrieve the N155° orientation proposed for the 2014
309 mainshock. Globally, the 2014 catalogue shows a wide variety of focal mechanisms and orientations,
310 which suggests that complex processes may be in play in this aftershock sequence (Fig. 3). Finally, as
311 the Ubaye catalogue and the 2014 aftershocks come from different origins, they will not be used
312 together, but in separate inversion process, for the stress-state reconstruction and the fluid-pressure
313 computation.

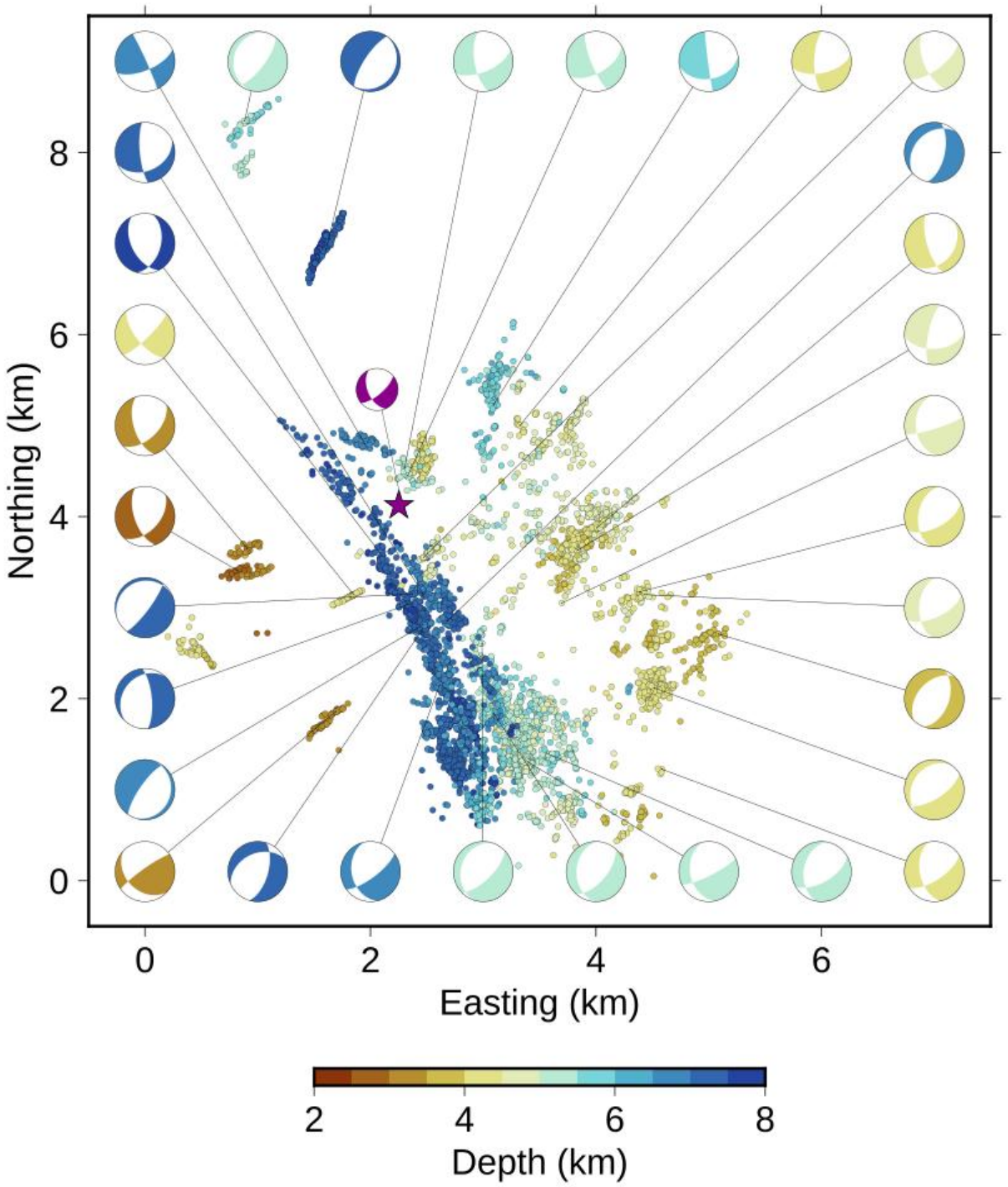

Figure 3: Map of the aftershocks relocated by De Barros et *al.* (2019) in the two months following the 7 April 2014 mainshock, with a subset of 32 (out of 100) computed focal mechanisms. The colours show the event depths. The purple star corresponds to the location of the 2014 mainshock with its focal mechanisms from Thouvenot et *al.* (2016).

4. Methods

4.1 Shape and orientation of the stress tensor

To estimate the fluid-overpressure required to trigger earthquakes, we use the focal mechanisms to reconstruct the stress-state orientation. To do that, we use the MSATSI program (Martínez-Garzón *et al.* 2014), which is a MATLAB version of the SATSI program developed by Hardebeck and Michael (2006). It is based on the Wallace (1951) and Bott (1959) assumption: the slip vector is assumed parallel to the maximal shear-stress. The stress-state is then determined through a grid-search inversion in order to maximize the shear-stress acting on the slip direction for all earthquakes. The MSATSI software requires as input the dip direction (strike+90°), the dip angle, and the rake, and computes the orientation of the principal stresses and the shape-ratio φ (Michael, 1984):

$$\varphi = \frac{\sigma 2 - \sigma 3}{\sigma 1 - \sigma 3} \quad (1)$$

The shape-ratio informs on the stress regime in the region associated with the orientation of the principal stresses (e.g. Gephart and Forsyth, 1984). Equivalently, we will use the R-ratio, defined as $R = 1 - \varphi$:

$$R = \frac{\sigma 1 - \sigma 2}{\sigma 1 - \sigma 3} \quad (2)$$

A R-ratio of 0 indicate a purely extensive regime, while values of 0.5 and 1 indicate strike-slip and compressive regime, respectively. We also calculate the uncertainties associated with the orientation of each stress component and shape-ratio, following the approach of Martínez-Garzón et *al.* (2016). For the 2014 relocated aftershocks catalogue, we used the mean uncertainty obtained when calculating the focal mechanisms to perturb the strike (+/- 25°), dip (+/- 12°), and rake (+/- 36°). These uncertainties are obtained by calculating 100 times a solution for each focal mechanism. As we

did not have information about the uncertainty associated with the published focal mechanism, we chose to perturb the parameters with a maximum of +/- 30°, which is consistent with the uncertainties we obtained for the 2014 relocated aftershocks. Then, randomly perturbing 100 times the strike, dip, and rake of each mechanism assuming a uniform distribution, we create 100 new catalogues, on which we apply 100 bootstraps operations. The inversions then lead to 10,000 values of shape-ratio, trend and plunge for each stress. From then, we calculate the mean and the standard deviation (Tab. S2, Fig. S5, Fig. S6).

We then aim at exploring how the stress-state is variable in space and time, calculating it for the different focal mechanism catalogues defined in previous section: full Ubaye Region, Ubaye Valley, Serenne area, Background seismicity, 2003-2004, 2012-2015, and 2014 relocated aftershocks. The results of these inversions are presented in the Results section.

4.2 Fluid-pressure

As mentioned in the introduction, fluid-pressure was highlighted as a driving process of the Ubaye Region seismicity. Two previous studies (Daniel *et al.* 2011; Leclère *et al.* 2013) calculated the fluid-overpressure needed to explain the 2003-2004 swarm and both assumed a stress-state with two horizontal components (σ1 and σ3) and one vertical component (σ2). However, in our case, the stress-state inversed for the 2012-2015 sequence (Fojtíková and Vavryčuk, 2018) has only one horizontal component (σ3) and two components (σ1 and σ2) neither vertical nor horizontal. Therefore, we generalize the approach used by Collettini and Trippetta (2007), Terakawa et *al.* (2010), Leclère et *al.* (2013), and Jansen et *al.* (2019), to calculate the fluid-overpressure.

As neither σ1 nor σ2 are vertical, we first express the vertical stress (σv) as a function of the principal stress components using Cauchy's equation. Assuming a lithostatic stress, we get:

$$\sigma v = cos^2(\theta_1)\sigma 1 + cos^2(\theta_2)\sigma 2 = \rho g Z \qquad (3)$$

With θ_1 and θ_2 corresponding to the angle between the vertical stress and the plunge of σ1 and σ2. ρ is the rock density taken at 2700 kg/m^3; g is the gravitational constant (rounded at 10 m/s²) and Z is the depth in meters.

Using the R-ratio (eq. 2) determined in the stress inversion, we can then reorganize eq. 3 to express σ1 and σ2 as function of σ3:

$$\sigma 1 = \frac{\rho g Z - R cos^2(\theta_2)\sigma 3}{(1-R)\left(cos^2(\theta_2) + cos^2(\theta_1)\right)} \quad (4)$$

$$\sigma 2 = \frac{\rho g Z - R(\rho g Z + cos^2(\theta_1)\sigma 3)}{cos^2(\theta_1) + cos^2(\theta_2) - R cos^2(\theta_2)} \quad (5)$$

We then assume that σ3 depends linearly on the depth (Z), such that:

$$\sigma 3 = AZ \quad (6)$$

Therefore, the only unknown left to determine σ1 and σ2 in eq. 4 and 5 is the coefficient A. To determine it, we first compute the shear and normal stress that apply on the faults. As we do not know yet which of the nodal planes inferred from the mechanism the fault plane is, both nodal planes are considered as possibly activated. The shear stress τ and normal stress σn are related to the principal stress components using Cauchy's equations:

$$\tau^2 = (\sigma 1 - \sigma 2)^2 l^2 m^2 + (\sigma 2 - \sigma 3)^2 m^2 n^2 + (\sigma 3 - \sigma 1)^2 n^2 l^2 \quad (7)$$

$$\sigma n = l^2 \sigma 1 + m^2 \sigma 2 + n^2 \sigma 3 \quad (8)$$

With l^2, m^2, and n^2, the cosine direction of σ1, σ2, and σ3 respectively.

We can then define the slip-tendency α for all nodal planes following Mattila (2015) and Jansen et *al.* (2019). This parameter describes how close the fault stress-state is from failure. A fault is at a critical stress state for α equal to 1, while it gets further from failure when α decreases. If we first assume that all faults are at a hydrostatic pressure, α is defined as:

$$\alpha = \frac{\tau}{\mu(\sigma n - \rho_f g Z)} \qquad (9)$$

379 With ρ_f=1000 kg/m^3 the water density and μ the friction coefficient. We here assume a standard
380 value of μ=0.6 (Byerlee, 1970).

381 When combining eq. 4, eq. 5 and eq. 6 with eq. 7 and eq. 8, the slip-tendency (eq. 9) only depends on
382 A. We then perform a grid search with A varying from 0 to ρg, with a step of 1 N/m^3. For each value
383 of A, we calculate the slip-tendency for all fault planes. We then select the best A-value, 1) given that
384 the slip tendency cannot be higher than 1, and 2) assuming that at least one event occurs with a fluid
385 pressure equal to the hydrostatic pressure, meaning that the most favourably oriented fault plane is
386 reactivated with hydrostatic fluid pressure (Terakawa *et al.* 2010; Terakawa *et al.* 2012). This
387 assumption tends to minimize the fluid pressure required to reach the reactivation threshold.
388 Therefore, we are looking for an A-value for which the maximal slip tendency is equal to 1. Once A is
389 determined, σ1, σ2, and σ3 (eq. 4, 5, and 6), as well as the stress state τ and σn acting on the faults
390 (eq. 7 and eq. 8) can be computed. Assuming cohesionless fault, we can then compute the fluid-
391 pressure that is required to induce failure using the Amontons' law:

$$PF = \sigma n - \frac{\tau}{\mu} \qquad (10)$$

392 For each event, a fluid-pressure value is computed for both nodal planes. To discriminate the fault
393 plane from the auxiliary plane, we could use either the misfit angle, which is the difference in the
394 direction between the slip and the maximal shear stress on the fault plane if considering the Wallace
395 and Bott assumption (Wallace, 1951; Bott, 1959), or the slip tendency (eq. 9), hence the lowest fluid
396 pressure, in the Mohr-Coulomb theory. For ~75% of the events, the plane with the highest slip
397 tendency is also the plane with the lower misfit angle or one of two planes with similar misfit angle
398 (see supplementary Fig. S7). For ~25% of the events, there is a discrepancy between the plane with
399 the lower misfit angle and the one with the highest slip tendency. As the (Wallace, 1951) and (Bott,
400 1959) assumption may show some limits (Kakurina *et al.*, 2019) and because we compute the full

stress tensor, we choose to keep as the fault plane the nodal plane the closest to failure, which is also the plane with the lowest fluid-pressure. The average misfit angles of the chosen fault planes is ~19° for the 2014 aftershocks (see supplementary Fig. S7), with only a few events (7%) with a misfit angle larger than 40°, but lower than 75°. To further validate that our fault plane determination is correct, we compare the chosen fault plane with the one proposed by the fault instability criterion (Vavryčuk *et al.* 2013). The fault instability criterion gives the nodal plane that is the closest to the rupture without resorting of stress-state computation. It only depends on the friction coefficient μ, the R-ratio, and the direction cosines from the principal stresses (Vavryčuk *et al.*2013):

$$I = \frac{\tau_r + \mu\,(\sigma_r + 1)}{\mu + \sqrt{1 - \mu^2}} \qquad (11)$$

where τ_r and σ_r are equal to:

$$\tau_r = \sqrt{l^2 + (2R-1)^2 m^2 + n^2 - (-l^2 + (2R-1)m^2 + n^2)^2} \qquad (12)$$

$$\sigma_r = -l^2 + (2R-1)m^2 + n^2 \qquad (13)$$

We find that 99% of the identified fault planes are similar by both approaches, confirming their determination.

The fluid-pressure depends on the depth as it is assumed to be higher than the hydrostatic pressure: $Ph = \rho_f g Z$ (14). To work with comparable values, we subsequently use the fluid-overpressure, defined as the part of fluid-pressure above the hydrostatic pressure (MPa):

$$\Delta PF = PF - Ph \qquad (15)$$

We can then define the overpressure ratio (%) by normalizing the overpressure by the hydrostatic pressure:

$$\frac{\Delta PF}{Ph} = \frac{(PF - Ph)}{Ph} * 100 \qquad (16)$$

Equivalently, another way to observe overpressure is through the pore-fluid factor (Sibson, 1990; Cox, 2016), which is the ratio of the pore-fluid pressure to the lithostatic pressure. We choose in this paper to use the overpressure ratio to compare with other studies using similar methods (e.g. Jansen *et al.* 2019), but results are shown in supplementary figures (Fig. S8, Fig. S9, Fig. S10, Fig. S11).

At the end, we obtain the fluid-overpressure needed to trigger slip on all fault planes of the focal mechanisms. We also estimate fluid-overpressure uncertainties by randomly perturbing 1000 times the strike, dip, and rake of the focal mechanisms on a range of 30° in a uniform distribution law. We then run the full inversion process on these 1000 perturbed catalogues, to reconstruct the stress-state and overpressures, leading to 1000 perturbed values of fluid-pressure (Fig. S12). Since the distribution is not symmetrical, we quantify the uncertainties for each event by measuring the overpressure range for which 34% (half of one standard deviation if the distribution was Gaussian) of the calculated values are above or below the initial fluid-pressure value. We then compute the median of these uncertainties for the different catalogues. We obtain an overpressure ratio uncertainty of -15% and +21% for Ubaye Valley, of -18% and +24% for Serenne, and of -17% and +15% for 2014 relocated aftershocks.

5. Results

5.1 Orientation and amplitude of the stress tensor

We determine the stress-state for the two months following the 2014 mainshock as well as for the full Ubaye Region, its two sub-areas (Serenne and Ubaye Valley) and the particular sequences (2003-2004 and 2012-2015 sequences). Fig. 4 summarizes the stress-state orientations calculated here and compares them to the published ones (Leclère *et al.* 2013; Fojtíková and Vavryčuk, 2018).

For the full Ubaye Region, we obtain a σ1 oriented N37° ± 8° and plunging 66° ± 6°, a σ2 oriented N192° ± 2° plunging 22° ± 6°, and a sub-horizontal σ3 oriented N285°± 1°. The σ3 is the only horizontal stress component and is tilted ~65° from the normal of the Frontal Penninic Thrust. The other two stress components, σ1 and σ2, are less well-resolved (Tab.S2, Fig.S6). Indeed, they can easily vary in a N190° vertical plane, which suggests that both components have similar amplitudes. Furthermore, the Ubaye Region shows strong variations in the topography, with more than 2000 m between valleys and mountain summits. As σ1 and σ2 depend on the depth, topographical effects may impact the plunge, as well as the amplitude, of these stress components.

We then refine this analysis by looking for spatial variations for the two sub-areas: Ubaye Valley and Serenne. In both cases, σ3 orientation is found similar to the Ubaye Region one while there are differences in the plunge for the other two components. Both σ1 and σ2 are within the N190° vertical plane, but σ1 is found subvertical (71°) in the Serenne area, while it shows a 41° plunge in the Ubaye Valley. Accordingly, σ2 is sub-horizontal (14°) and more vertical (49°) in the Serenne and Ubaye Valley, respectively. As mentioned above, this difference might be (partly) due to topographical effects.

The stress-state orientations for the two main sequences of 2003-2004 and 2012-2015 and for the remaining focal mechanisms (background seismicity) in the Ubaye Valley are found very similar to the Ubaye Valley one (Fig. 4, Tab.S2). Some very limited differences (<5°) in the plunge of σ1 and σ2 might be explained by the variation of topography or uncertainties in the computation. Same observations can be noticed when looking specifically at the aftershocks of the 2014 event: the stress-state does not show significant differences with the other ones.

Moreover, the stress-state orientation we determined are similar to the ones computed by Fojtíková and Vavryčuk (2018), the differences being within the uncertainty range. The stress-state computed by Leclère et *al.* (2013) for the 2003-2004 sequence shows a subvertical σ2, while they use the same catalogue of mechanisms as Fojtíková and Vavryčuk (2018) who found plunging of 49° (Tab.S2).

We also retrieve similar R-ratio ≈ 0.31, for the different catalogues (Tab.S2). Their values are also compatible with the ones found by Leclère et *al.* (2013) for the 2003-2004 swarm and by Fojtíková and Vavryčuk (2018) for the 2003-2004 and 2012-2015 swarms with a mean R-ratio ≈ 0.29. This value indicates extension and strike-slip regime in this region, which is in agreement with geodetic observations.

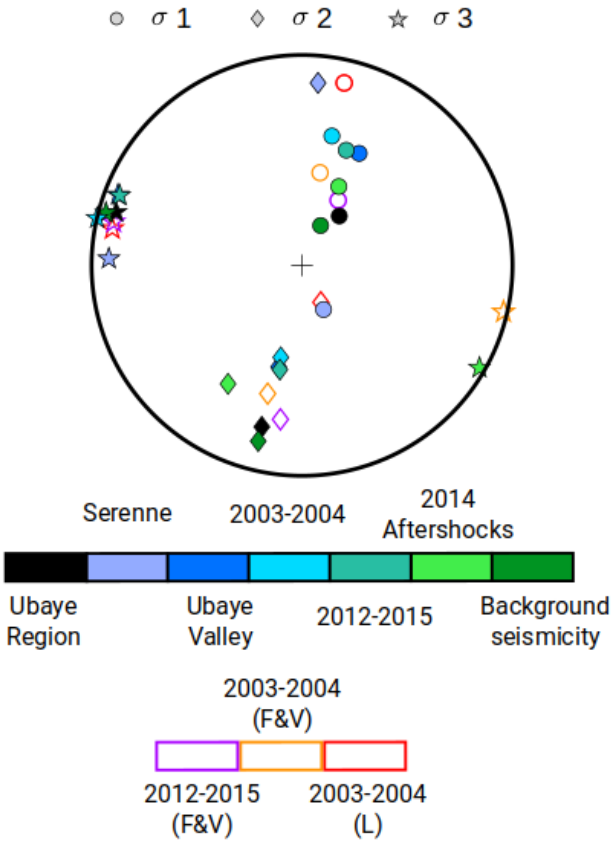

Figure 4: Polar view of the stress-state orientations (circle for σ1, diamond for σ2, and stars for σ3). Computed stress-states are shown as filled symbols coloured by regions (full Ubaye Region, and its two sub-areas: Serenne and Ubaye Valley, Fig. 2b); or periods (2003-2004 swarm, 2012-2015 sequence, background seismicity, Fig. 2c; and 2014 aftershocks, Fig. 3). The red, pink, and purple unfilled symbols correspond to published stress-states: "F&V" for Fojtíková and Vavryčuk (2018); "L" for Leclère et *al.* (2013).

The magnitude of the principal stresses is then determined (Figs 5a, c, and e, for Ubaye Valley, Serenne, and 2014 relocated aftershocks catalogues, respectively). In all cases, they are found to be very similar, as $\sigma3 \approx 15*Z$ (MPa), with the depth Z in km. Equivalently, the deviatoric stress is found to increase with depth as $\sigma1-\sigma3 \approx 13*Z$ (MPa). As expected, σ1 is close to σ2, even if their magnitudes vary slightly among cases, as the stress-state inversion reveals differences, albeit small, in their plunge. Once again, these differences may be explained by topographic effect, as the 2014 aftershocks occurred below the Parpaillon massif, which culminates at 3000 m.

In summary, the stress-states and the R-ratio are found similar for the different catalogues, and consistent with previously published results. Therefore, anomalies in the stress-state orientation or magnitudes cannot explain the swarm behaviours or the complex aftershock sequences of the 2014 earthquake. As the stress-state seems spatially homogeneous constant, we then mainly focus on the Ubaye Valley, Serenne area, and 2014 aftershocks to explore their fluid-overpressure behaviour.

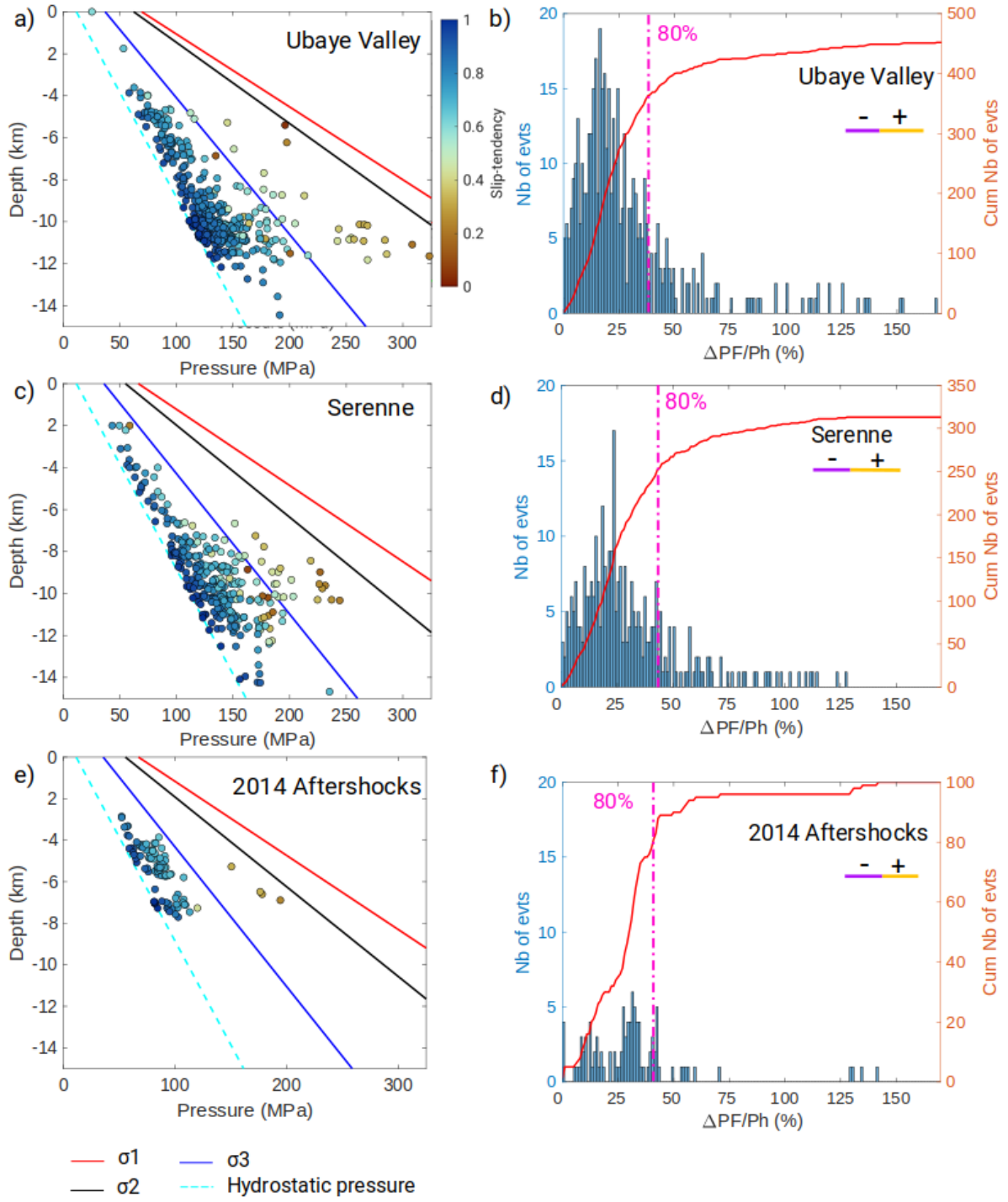

491

492 Figure 5: Fluid-pressure versus depth (left panels: a, c, e) and histograms of overpressure ratios (right
493 panels: b, d, f), for the Ubaye Valley (a, b), the Serenne area (c, d), and the 2014 aftershocks (e, f). In
494 a), c), and e), the dots show the fluid-pressure required to reactivate the selected fault planes
495 coloured by the slip-tendency at hydrostatic pressure. The depth is below sea level. The light blue,
496 blue, black, and red lines correspond to the hydrostatic pressure, σ3, σ2, and σ1, respectively. In b),

d), f), the histograms show the number of events per overpressure ratio (%), while the red lines show the cumulative number of events. The purple and yellow bars correspond to the common negative and positive uncertainty that are found to all the fluid-overpressure values. The pink dashed line shows 80% of the cumulative number of events. The number of earthquakes as function of pore-fluid factor is also available in Supplementary Materials (Fig. S8).

5.2 Fluid-overpressure

Figs 5a, c, and e shows the fluid-pressure computed for the nodal planes the closest to rupture. These planes are assumed to be the fault planes of the seismic event. This assumption is supported by the correlation of our results with the values of the fault instability criterion described in section 4.2. All computed fluid-pressures are equal or above the hydrostatic pressure, as we assumed a minimal hydrostatic pressure. Only a few events require an overpressure higher than σ3. In this case, failure might imply some tensile component. Some of the published focal mechanisms used in our catalogues have quality indexes (Mathey *et al.* 2021a). We find that events with a fluid-pressure value higher than σ3 have the lowest quality index (Figs S11b and d). We then discard events with a fluid-pressure value higher than σ3 from the analysis as their mechanisms might be fraudulent with large errors.

To get rid of the dependency on depth, we also look at the overpressure ratios. We consider that the overpressure required to trigger the events is significant when it is higher than the computed minimum uncertainties: 15% for Ubaye Valley (Fig. 5b), 18% for Serenne (Fig. 5d), and 17% for the 2014 aftershocks (Fig. 5f). Considering these uncertainties, 68% (Ubaye Valley), 61% (Serenne), and 69% (2014 aftershocks) of the events required overpressure to be triggered, leading to median overpressure ratio of 27%, 30%, and 32% for the Ubaye Valley, Serenne, and 2014 aftershocks, respectively. In absolute values, at least 46% of the events require fluid-overpressure less than 45

MPa for the Serenne area. For the 2014 aftershocks catalogue, at least 60% of the events need less than 27 MPa of overpressure. 48% of events require less than 38 MPa of overpressure for the case of the Ubaye Valley area (Fig. S14). The three catalogues lead to similar values of median overpressure: 24 MPa, Ubaye Valley catalogue; 30 MPa, Serenne catalogue; 20 MPa, 2014 relocated aftershocks catalogue.

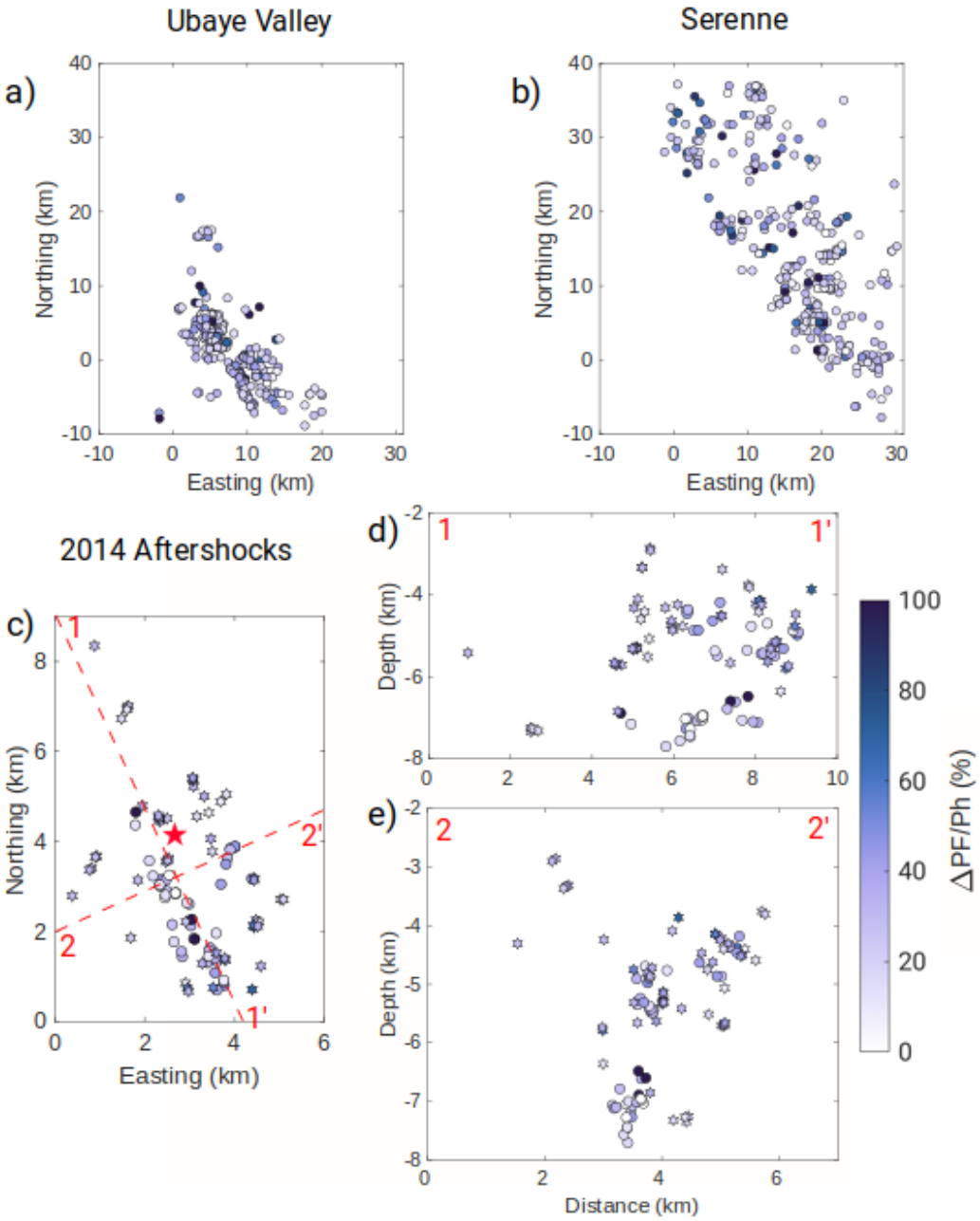

Figure 6: Map view of the overpressure ratio (%) for the Ubaye Valley (a), the Serenne area (b), and the 2014 relocated aftershocks (c). In c), the red star shows the location of the 2014 mainshock

(Thouvenot *et al.* 2016). The dashed red-lines show the cross-sections that are used in d) and e). In c), d), and e), the hexagrams and circles correspond to events belonging to swarm-like clusters and aftershock-like clusters, respectively. The depth is below sea level. The same figure, with pore-fluid factor as function of location is available in Supplementary Materials (Fig. S9).

We then analyse the spatial distribution of the reconstructed fluid-pressure (Fig. 6), but we do not see any clear tendency. Indeed, despite an important scattering in overpressure ratios, no consistent anomalies are observed on map view, neither for the 2014 relocated aftershocks (Fig. 6c) nor for the Ubaye Valley and Serenne areas (Figs 6a and b). The families that composed the 2014 aftershocks were classified by De Barros et al. (2019) into aftershock-like or swarm-like behavior based on their space, time and magnitude distribution (Figs 6c, d, and e). The median value of overpressure ratios for aftershock-like clusters is slightly lower (27%) than the one for swarm-like clusters (31%). This is to be expected, as swarms are commonly driven by fluid-driven processes. However, no clear difference is observed spatially between events belonging to clusters with a different behavior (Figs 6c, d, and e).

There is also no clear dependency between the depth and fluid-overpressure for the Ubaye Valley (Fig. 7a), as the median values are found nearly constant between 4-12km depth. For the 2014 aftershocks, we also observe a constant fluid-overpressure as a function of depth (Fig. 7c). Therefore, for both catalogues, the overpressure does not seem to depend on the hydrostatic pressure. On the contrary, for the Serenne area, the reconstructed overpressure seems to increase with depth, and therefore with the value of the hydrostatic level. This difference in behaviour between Serenne and Ubaye Valley might suggest a difference either in the geological context or in the driving processes.

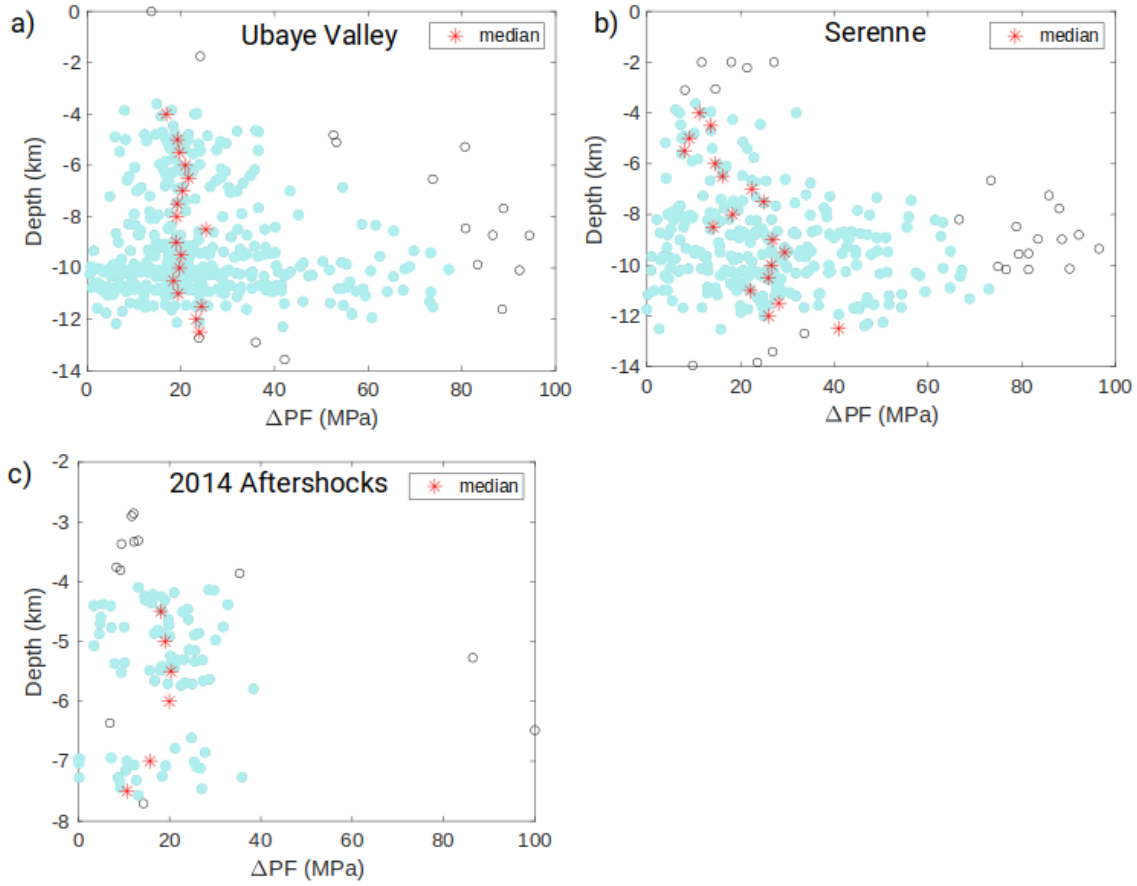

552

553 Figure 7: Fluid-overpressure (MPa) versus depth for the Ubaye Valley (a), the Serenne area (b), and
554 the 2014 relocated aftershocks (c). Each dot corresponds to a focal mechanism and depth is directly
555 associated to each solution. Each dot corresponds to an event with a computed focal mechanism.
556 Red stars show the median value of the fluid-overpressure on a 500-m-depth sliding window with a
557 250 m overlap. Only median values calculated with at least 5 events are represented. Empty circles
558 correspond to events having an overpressure above σ3, and are thus discarded for the median
559 calculation. The depth is below sea level.

560

561

562 Fig. 8 represents the overpressure ratio as a function of the event magnitude (ML) for the different
563 areas and seismic sequences. For the sake of homogeneity, we use the local magnitude (ML)
564 computed by the LDG (Duverger *et al.* 2021) for all events in our focal mechanism catalogues. In both

565 the Ubaye Valley and the Serenne areas, the median of the reconstructed fluid-pressure values does
566 not depend on the event magnitude. The same is observed for the overpressure (Fig. S15).
567 Particularly, the largest events need similar level of fluid-pressure as the average for the smallest
568 ones. The same observation is made when focusing on particular sequences, such as the seismicity in
569 2012 (Fig. 8d). The reconstructed overpressure ratio appears more scattered for low magnitude
570 events (ML<2.5) as the number of events decreases with magnitude. This might also indicate a
571 variability in the processes or a larger uncertainty on the focal mechanisms for lower magnitude
572 events. However, the mainshock that started this sequence (ML4.8, 26/02/2012) needs ~30% of
573 overpressure ratio (overpressure of ~35 MPa, Fig. S15d*)*, which is above the median value of the
574 reconstructed overpressure ratio and one of the largest for events of magnitude larger than 2.5 (Fig
575 8d). This suggests that fluid-pressure is required to trigger both large and small events, whatever
576 their magnitude.

577 To confirm this statement, we look in detail at fluid-pressure uncertainties for particular
578 earthquakes. Figure 9 represents the distribution of fluid-overpressures obtained by perturbing 1000
579 times the source fault properties (strike, dip, and rake) of all events (see section 4.2). For each of
580 these perturbed catalogues, we run again the full analysis, including the inversion for the stress-state
581 orientation, amplitude and the fluid-overpressure. We then focus on 9 events with magnitude ML
582 from 2.9 to 5.2. Two of these earthquakes occurred in the Serenne area (Figs 9b and c) in Feb. 1996,
583 and 2000, two were from the background seismicity of the Ubaye Valley (Figs 9a and f) in Jan. 1996
584 and 2005, and two happened during the 2003-2004 swarm (Figs 9d and e). The last three events are
585 the largest earthquakes of the 2012-2015 sequence, which occurred on 26/02/2012 (Fig. 9g),
586 07/04/2014 (Fig. 9h), and 06/11/2015 (Fig. 9i). Some of these events unambiguously need fluid-
587 overpressure to reach the reactivation criterion (Figs 9b, c, e) as their distributions show a clear peak
588 around a high fluid-overpressure value. The overpressure distributions of the earthquakes occurring
589 in 2003 and 2012, (Figs 9d, g and h) are wider but still suggest an activation by fluid-pressure.
590 However, this is not as clear for the Jan. 1996, 2009 and 2015 events (Figs 9a, f and i) for which their

591 distribution is squeezed toward low values of overpressure. Overall, by considering uncertainties, the
592 data presented in Fig. 9 confirm the need for overpressures triggering earthquake, even if the
593 reconstructed values of overpressures might be variable. Therefore, this confirms that even the
594 largest earthquakes are likely to have been caused by fluid pressure, whether they occurred as part
595 of a swarm or as an isolated earthquake.To refine this observation, we look at how the overpressure
596 ratio evolves with time within a swarm and during an aftershock sequence (Fig. 10). During the 2003-
597 2004 swarm (Fig. 10a), the overpressure ratio varies in time at high level without following a clear
598 pattern. On the contrary, during a mainshock-aftershocks sequence, like in 2012 (Fig. 10b), high
599 values of overpressure ratio (up to 68%) are observed at the beginning of the sequence, right after
600 the mainshock. It then slowly decays in the next 6 months, to stabilize below 30% (Fig. 10b, black
601 line). Therefore, it suggests that the difference between a swarm and a mainshock-aftershock
602 sequence may be more related to the evolution of the fluid-overpressure in time rather than to its
603 absolute values. Both required overpressure in their driving process, but the overpressure ratio
604 decays with time in the mainshock-aftershocks sequence and not in a swarm episode.

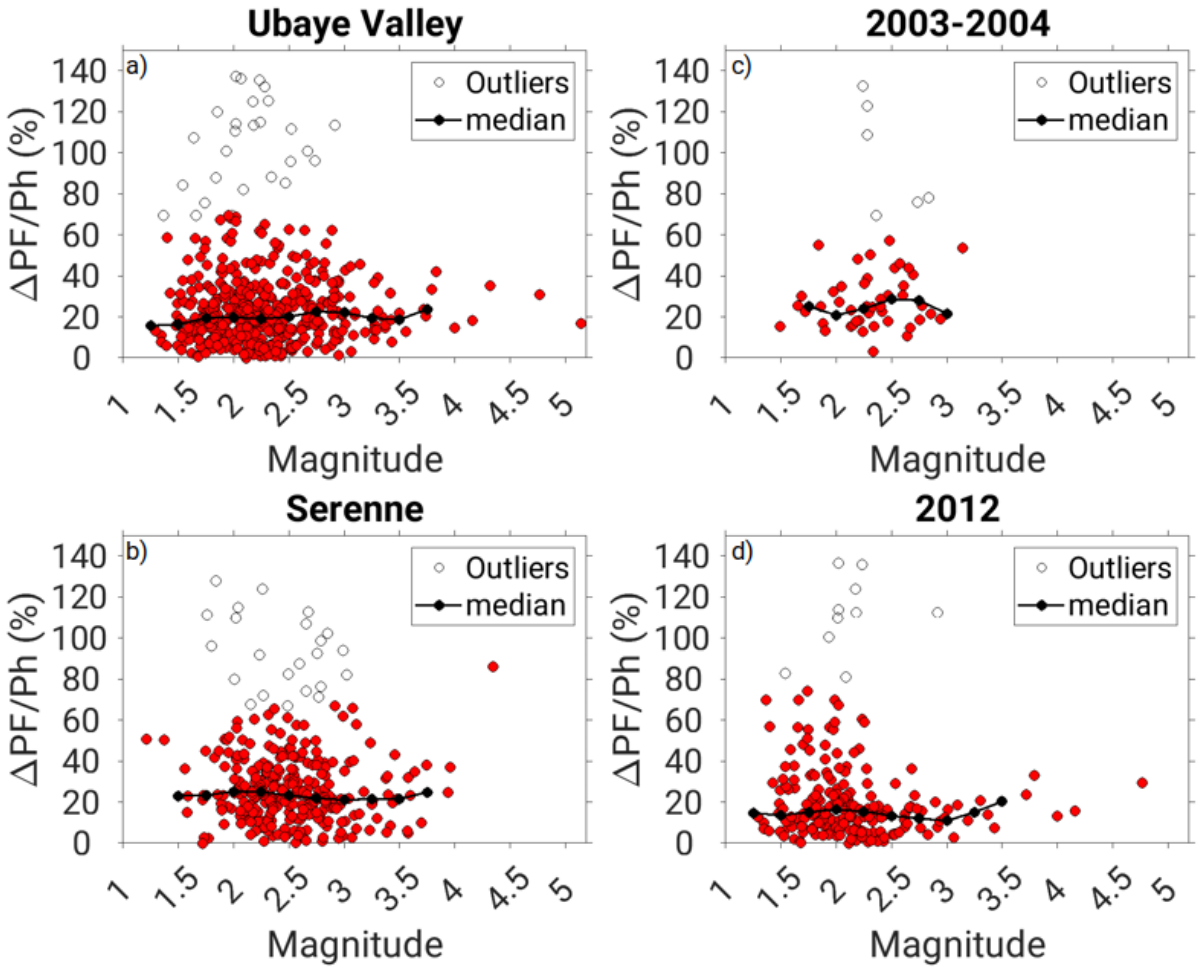

Figure 8: Overpressure ratio as function of local magnitude for the Ubaye Valley (a), the Serenne area (b), the 2003-2004 swarm (c), and after the 2012 mainshock (d). The local magnitude comes from the LDG catalogue (http://www-dase.cea.fr). The empty circles show events with overpressure ratio higher than σ3, which are therefore discarded from the analysis. The black line shows the floating median calculated for every 0.25 bin of magnitude with at least 5 events. The same figure, with pore-fluid factor as function of magnitude is available in Supplementary Materials (Fig. S10).

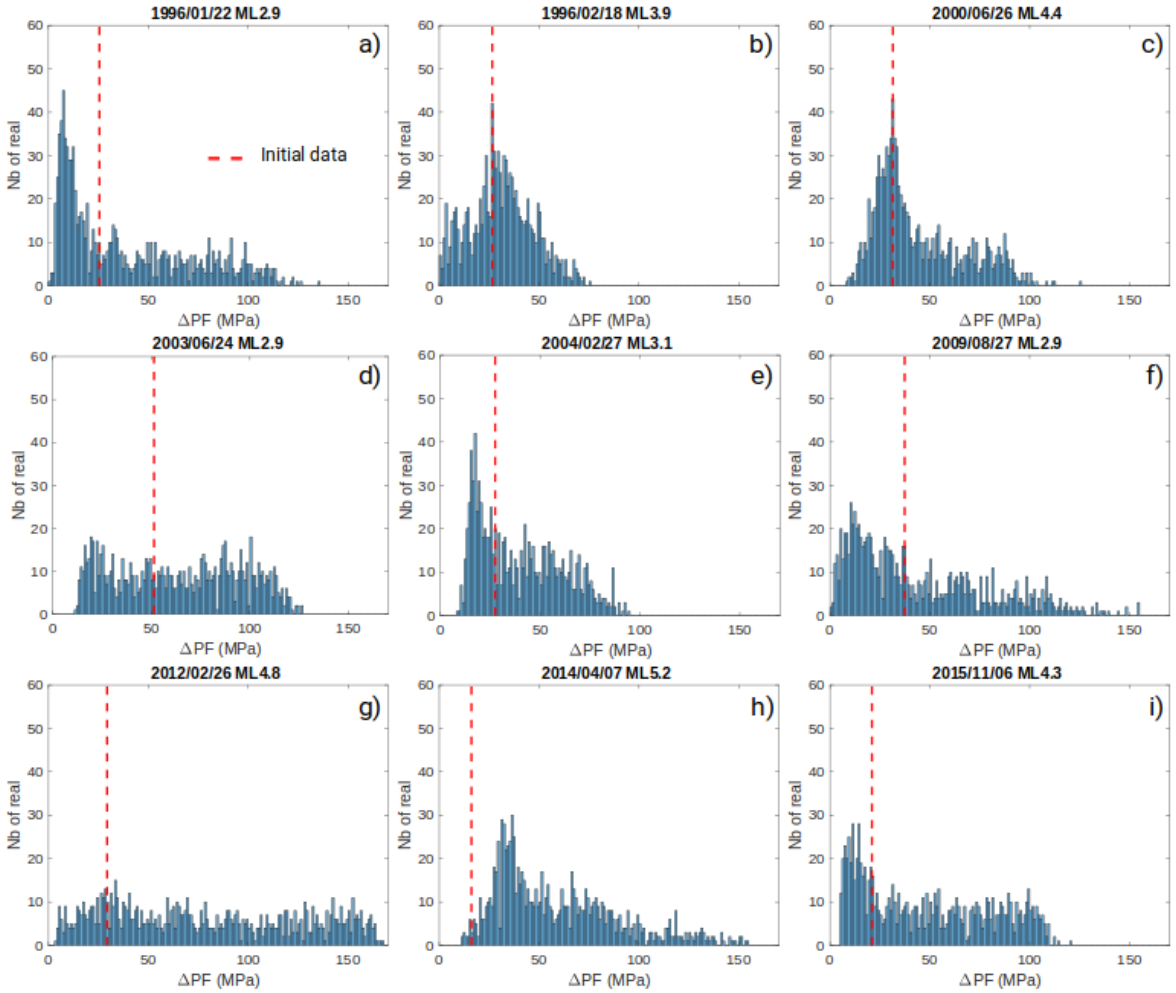

Figure 9: Distribution of overpressure obtained by the inversion of 1000 perturbed catalogues of focal mechanisms. For each perturbed catalogue, the stress-state is first inverted before being used in the pressure calculation (see section 4). The number of realizations is the number of perturbed catalogues leading to fluid-overpressure value in a 1 MPa bin. Results are shown for 9 selected earthquakes occurring in the background seismicity (a, f), along the Serenne fault (b, c), during the 2003-2004 swarm (d, e) during the 2012-2015 sequence (g to i). The local magnitude of the events is taken from the LDG catalogue (http://www-dase.cea.fr). The dashed-red line corresponds to the initial value of fluid-overpressure calculated using the unperturbed catalogue.

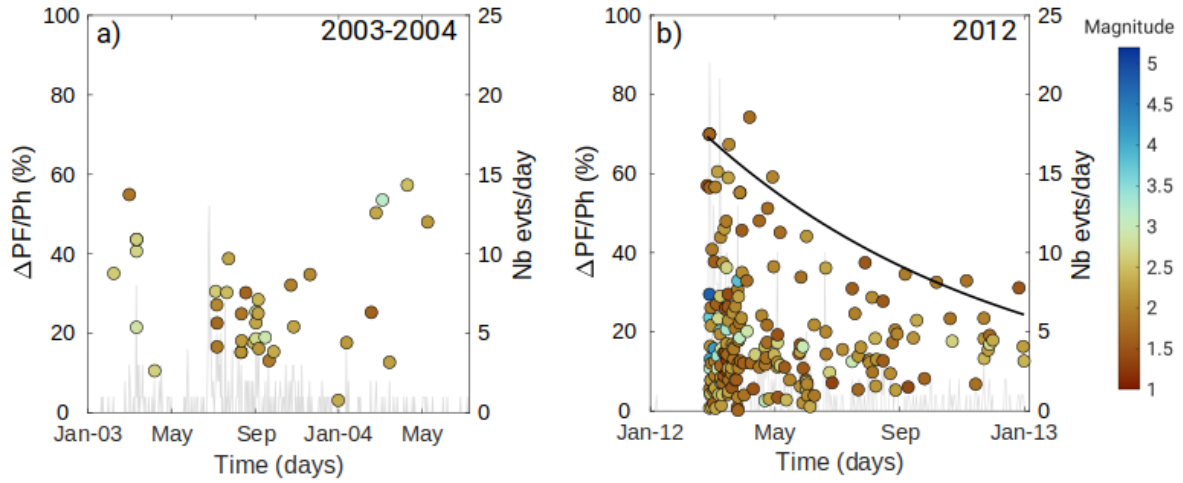

Figure 10: Overpressure ratio as function of time for the 2003-2004 swarm (a) and after the 2012 mainshock (b). The colour corresponds to the local magnitude from the LDG (Duverger *et al.* 2021). The grey bars (right axis) show the temporal distribution of the earthquakes, from the LDG catalogue (http://www-dase.cea.fr). Only the events with an overpressure ratio lower than σ3 and in the LDG catalogue are represented. In b), the black line fits the 90th percentile maximum overpressure ratio value every month following an exponential law. The same figure, with pore-fluid factor as function of time is available in Supplementary Materials (Fig. S11).

6. Discussion

From the focal mechanisms, we reconstructed the stress-state and the fluid-overpressure that trigger earthquakes for different areas and time periods in the Ubaye Region. We showed that the majority of the events need overpressure at median value of 20-30 MPa, or equivalently at 27-32% of the hydrostatic pressure. We also showed that there are no significant spatial variations of either the stress-state nor the fluid-overpressure. Even the largest events are triggered by fluid-pressure, but the time evolution of fluid-overpressure is different for a mainshock-aftershocks sequence or for a swarm sequence.

In this discussion, we first analyse the different sources of uncertainties that may impact our results. Then, we discuss the stress state and overpressure results, in order to propose an interpretative mechanism for fluid-driven aftershock seismicity and swarms.

6.1 Source of uncertainties

The main uncertainties we have to deal with come from the accuracy of the focal mechanisms, as they are used to compute both the stress state and the overpressures. However, we do not have precise information on the uncertainties of the focal mechanisms we used, as they come from various origins. We therefore have to assume a range of uncertainties. Then, the statistical approach based on the focal mechanism's perturbation (section 3.2) allows the propagation of those uncertainties through the full workflow to estimate the stress-state and fluid-pressure uncertainties. The error bars in Fig. 5 or the distribution of overpressures for the 1000 perturbed catalogues (Fig. 9) show that the reconstructed overpressures may vary, but that the requirement of fluid pressure is reliable.

We show that the reconstructed fluid-pressures, on average, do not show horizontal spatial variations (Fig. 6). On average, they are also found constant with depth (Fig. 7) in the Ubaye Valley, while they seem to increase with depth in the Serenne area. These observations are based on our confidence in the location of events. However, we do not have information on location uncertainties the focal mechanisms for the regional catalogues. On the contrary, the 2014 aftershocks were relocated through a double-difference algorithm, with limited relative location uncertainties (De Barros *et al.* 2019). Using this specific catalogue, we do not observe any horizontal spatial pattern (Fig. 6c) but a constant trend with depth (Fig. 7c), similarly to the Ubaye Valley patterns. By extrapolation, we may conclude that, on average, the location uncertainties do not likely bias the spatial results.

In our analysis, we focused only on the variation of fluid-overpressure (ΔPF). However, to reach failure, we could also have an increase of shear stress (overstress, Δτ). Particularly, the aftershocks that are close from the 2014 mainshock can be reactivated by Coulomb stress transfer from the mainshock (Stein, 1999). In this case, the overstress should be smaller than the stress drop of the mainshock, which is assumed to be close to 10 MPa (Kanamori and Anderson, 1975). From eq. 10, the required overstress Δτ can be expressed as a function of the computed ΔPF:

$$\Delta\tau = \mu\Delta PF \qquad (17)$$

For most of the events (~68%), the overstress that is needed is above 10 MPa. Therefore, even if part of the required perturbation might be due to shear-stress increase, the reconstructed values suggest that fluid-overpressure is anyway required for a large majority of events. As we could not discriminate between shear-stress increase and fluid-overpressure, and for sake of simplicity, we therefore focus our interpretations on fluid-driven processes.

6.2 Stress-state

The reconstructed stress-state shows a horizontal σ3, striking ~N280°, and σ1 and σ2 in a vertical plane oriented ~N190°. Their plunge in this plane varies, as σ2 is found between sub-horizontal and 45° dipping. Their reconstructed stress magnitude is however very close (Fig. 5), meaning that the plunge variations can be easily explained, by, for example, topographical effect. In NE Japan, beneath low-altitude areas, the reverse regime (σ3 vertical) is dominant while high altitude areas show a strike-slip regime (σ2 vertical) (Yoshida et al. 2015). Similarly, the Ubaye Region shows large altitude differences (~2000m) between summits and valleys. Therefore, additional weight from high summit mountains may increase the vertical stress, leading to a σ1 plunge closer to the vertical beneath summits, while it will get more horizontal beneath valleys.

The inversion of focal mechanisms for the different sub-areas lead to very similar stress-state, in both its orientation and its amplitude. The stress-state orientation is consistent with results from other studies (Fojtíková and Vavryčuk, 2018). Particularly, similar stress-states are found for the Serenne area, characterized by well-identified faults and diffuse seismicity, and for the Ubaye Valley where recent seismicity occurred as swarms or mixed sequence along hidden faults. Therefore, large spatial heterogeneity in the stress-state cannot be used to explain the variability in the seismic behaviours, even if we cannot discard very localized variations (Heap *et al.* 2010) that are below the resolution we have with focal mechanisms inversion.

We do not observe differences in the stress-state either when using the full time period or focusing on perturbed periods of dense seismic activity, such as during the 2014 aftershocks sequence. We could have expected a perturbation of the stress-state because of aseismic afterslip that drives the aftershocks. For example, Duboeuf et *al.* (2021) observed perturbed stress-state associated with fault reactivation by fluid-injection in decametric experiments. As more than 90% of the deformation was observed to be aseismic, they attributed the stress perturbation to the aseismic slip. Same conclusion was reached by Schoenball et *al.* (2014) during a geothermal exploitation. Unlike aseismic slip, fluid-pressure may not influence the determination of stress-state orientation. Indeed, as fluid-pressure could trigger slips on faults that are badly oriented in whatever direction toward the stress-state, the focal mechanisms inversion leads to an average stress-state, similar to an unperturbed one. Therefore, the constant stress-state we reconstructed suggests that large aseismic slip is not a likely mechanism to explain the high rate of seismicity. Even if the spatial resolution brought by the focal mechanisms cannot allow us to conclude on the presence of aseismic slip at small-scale, fluid-pressure seems to be the dominant process.

6.3 Fluid-pressure values

711 Several studies (Jenatton *et al.* 2007; Daniel *et al.* 2011; Leclère *et al.* 2013; Thouvenot *et al.* 2016; De
712 Barros *et al.* 2019) highlighted the role of fluid-pressure as the main driving process required to
713 explain the high rate of seismicity for the 2003-2004 swarm and the 2012-2015 aftershocks. We here
714 find that significant overpressure (above uncertainties) is required for most of the events (~77%),
715 with a median overpressure of 22 %. This observation is independent of the areas, as both Serenne
716 area, and Ubaye Valley area, show similar pressure levels, despite their different seismic behaviour.
717 This need for fluid-pressure is also seen for all types of seismic sequences, including mainshocks,
718 their following aftershocks, or swarm sequences (Figs 6d and e). On average, we find that the
719 overpressure ratio should be up to 40% and, equivalently, that the fluid-overpressure is up to 70
720 MPa, even if 80% of the events need less than 40 MPa. Other fluid-overpressure analysis was carried
721 out in the Ubaye Valley for the 2003-2004 swarm by Leclère *et al.* (2013). Using a Mohr-Coulomb
722 analysis, they obtained a required overpressure of up to 55 MPa, consistently with the ones we
723 found for the 2003-2004 period and for the other periods and areas.

724 Determination of fluid-overpressure was also done for other swarms in different contexts. The Mogul
725 swarm (2008, e.g. Ruhl et *al.* 2016) occurred in the Nevada state in a hydrothermal context. Using a
726 similar methodology as the one used here, Jansen et *al.* (2019) computed the fluid-overpressure
727 required to trigger the Mogul seismicity and confirmed their results with numerical modelling. They
728 obtained a median overpressure ratio of 42% that is more than for the full Ubaye Region (22%). This
729 difference might be linked to the presence of hot springs in the Mogul swarm area, which revealed
730 an elevated fluid-pressure level in the medium. They also found fluid-overpressure up to 30 MPa,
731 which is consistent with our values. For some events, they also found fluid-pressure higher than the
732 minimum magnitude stress component. They proposed that other processes (static stress transfer,
733 transient poroelastic stress changes, aseismic slip) should explain the high fluid-pressure values
734 obtained.

735 Fluid-driven process was also proposed for the Vogtland/Western Bohemia area that was struck by
736 several swarms (e.g. Heinze *et al.*, 2017). Kurz et *al.* (2004), using finite element modelling, calculated
737 the fluid-overpressure required to trigger the different earthquake swarms in the 1990-1997 period.
738 They estimated a need of fluid-overpressure up to 50 MPa, with some events needing overpressure
739 as high as 150 MPa, which they deemed unrealistic. Hainzl et *al.* (2012) also computed fluid-
740 overpressure for the beginning of the 2008 Western Bohemia swarm. Using stress changes and
741 hydrofracture model, they estimated a need of 20-30 MPa of fluid-overpressure. Terakawa et *al.*
742 (2010) used a similar method as Leclère et *al.* (2013) to estimate the fluid-overpressure required for
743 the Mw6.3 L'Aquila earthquake and its foreshocks-aftershocks. They found a range of fluid-
744 overpressure between 20 to 50 MPa. In this case, even if a strong earthquake was likely induced by a
745 fluid-driven process, the range of fluid-overpressure is similar to the one inferred on natural swarms
746 where the magnitude rarely exceeds ML4 (Ma and Eaton, 2009). Therefore, it seems that, for natural
747 swarms induced by fluids, fluid-overpressure with values up to ~50 MPa is observed.

748 During injection-induced swarms, the behaviour of the fluid-pressure and therefore the fluid-
749 overpressure is monitored. Baisch et *al.* (2010) observed the evolution of the fluid-pressure in a case
750 of fluid injection experiments in Soultz-sous-Forêts (France). They observed a fluid-overpressure up
751 to 18 MPa at the reservoir depth (~4km). For another experimental zone, Basel Switzerland,
752 Terakawa et *al.* (2012) retrieved a required fluid-overpressure up to 30 MPa. These values of fluid-
753 overpressure in injection-induced swarms are also similar to the ones we found here and for other
754 natural swarms (Mogul, Vogtland/Western Bohemia).

755

756 6.4 Origin of pressurised fluids

757 One of the main questions that remains when involving fluids in the driving processes is where they
758 come from and how they get pressurized. A first possibility is the meteoric origin. Some swarm

sequences (e.g. Mt Hochstaufen, Hainzl et *al.* 2006; Mogul, Jansen et *al.* 2019) were explained by the infiltration of rainwater in the medium that increased the fluid-pressure and triggered the seismicity. For the 2003-2004 swarm, Leclère et *al.* (2012, 2013) also proposed that meteoric fluids infiltrated in the Argentera massif and then flowed to the seismic area of the 2003-2004 swarm. The difference in elevation between the Argentera summits (>2500 m) and the Ubaye Valley (~1000 m) allow a fluid-pressure to develop in the swarm area, assuming that faults are highly permeable with the Embrunais-Ubaye nappes acting as cap-rock. This is consistent with the chemical analysis of a geothermal spring located 20 km south-east of the Ubaye Valley (Bagni di Vinadio, Baietto et *al.* 2009; Perello et *al.* 2001). Water is shown to have a meteoric origin, before flowing up to ~5km depth, close to the seismicity depth. Such a model was also used to explain the seismicity of the Mogul swarm, which also occurred below a valley surrounded by high summits (Ruhl *et al.* 2016; Jansen *et al.* 2019). Following this idea, we could expect to see a spatial tendency in the overpressure distribution, with a decrease of overpressure with the distance to the Argentera and Pelvoux summits. This is not observed, as the overpressure does not show any clear spatial tendency. Moreover, as such a model requires a cap-rock to allow pressure to develop, the seismicity away from the Embrunais-Ubaye nappes, as the Serenne earthquakes, should not require fluid-pressure. Finally, if the Embrunais-Ubaye nappes acted as a cap-rock, the seismicity would dominantly develop just below it, at ~2 km depth below sea level. This is not observed, as the seismicity mainly equally develops from ~4 to 12 km below sea level.

Another possibility is the presence of a deep reservoir. This was proposed to explain the seismicity of several swarms (Duverger *et al.* 2015, 2018; Hainzl *et al.* 2016; Jansen *et al*. 2019; De Barros *et al.* 2020; Ross *et al.* 2020). The reservoir is at first impermeable, then due to some perturbations (stress-change, tectonic loading ...), it becomes permeable by place, which releases the fluids that then flow in the medium. The fluids could migrate either upward (Duverger *et al.* 2018; Jansen *et al*. 2019) or horizontally (Farrell *et al.* 2010). This is for example the main interpretation for the complex seismic behaviours in the Corinth rift. The low-permeability Phyllade nappe at 6-8 km depth leads to

pressurized fluid beneath it. Its failure then allows fluid-pressure to diffuse, triggering swarm seismicity (Duverger *et al.* 2018). In the Ubaye Valley, the reservoir needs to be of the scale of the studied region, as fluid-pressure is required for the majority of the events. This might not be likely, as, in this case, overpressures are expected to be at similar values and not scattered as observed. Moreover, a hydrological barrier at depth is required to maintain the reservoir at high pressure, but there is no geological evidence for such a layer at a regional scale. However, a smaller reservoir beneath the starting location of the 2003-2004 swarms could explain it, as seismic migrations might then be related to fluid flow (Shapiro *et al.* 1997).

A third possibility to explain the fluid-pressure is that the fluids are locally pressurized within the faults, through a model of fault-valve behaviour (Sibson, 1990) or creep-compaction (Leclère *et al.* 2015). If the fault is sealed by a hydraulic barrier with low-permeability, the fluid-pressure tends to increase from a hydrostatic pressure to a lithostatic one. This increase of pressure then promotes the fault slip. Doing so, the hydraulic barrier in the fault may break, causing the over-pressurized fluids to migrate upward. This model was used to explain different swarms (e.g. Cahuilla swarm, Ross et *al.* 2020; Southern California, Ross and Cochran, 2021; Haenam swarm, Son et *al.* 2021; Mammoth Mountain, Shelly et *al.* 2015). A remaining question is the nature of the hydraulic barrier within the fault. There is so far no evidence of a layer in the basement at depth that could produce a low-permeability cap-rock. Leclère et *al.* (2015) suggested that creep compaction of the fault can lead to impermeable barriers in the fault zone. Alternatively, the presence of clay within the faults by direct chemical and physical alteration may produce hydraulic barriers. Finally, the presence of Embrunais-Ubaye nappes, which lie on clay-rich materials (Lias, Trias, and Callovo-Oxfordien) may prevent a fast overpressure dissipation, which may explain why seismicity organizes as swarms in the Ubaye Valley and not in the crystalline massifs around (Argentera and Pelvoux). We therefore detail how such a model may be applied in the Ubaye Valley in the next section.

6.5 Mechanisms for fluid-driven aftershock seismicity and swarms

The fault valve behaviour is the model we use to explain the different types of seismicity, and particularly the high rate of aftershocks observed after the 2014 events. As the required fluid-pressure decreases with time, the mainshock is likely to initiate the fluid-pressure diffusion. Initially, the fluids are trapped by hydraulic barriers, made of clay lenses from gouge materials or mineral recrystallization, within the 2014 mainshock fault as it may tend toward lithostatic pressure (Fig. 11, Initial State). The fluid-pressure then increases as it equilibrates with the confining stress through time, and may tend toward the lithostatic pressure. This leads the faults reaching the reactivation criterion, generating the 2014 mainshock, which also breaks the hydraulic asperities. The pressure then readjusts along the rupture plane, and trigger events on smaller faults close to or above the main fault plane (Fig. 11, Perturbed State). This is consistent with a fluid-overpressure constant with depth, as observed in Fig. 7c. The fluid-pressure, together with Coulomb stress transfer, therefore participates in the triggering of the aftershocks close to the main fault plane, as fluid-pressure seems also required for some of the deep events around the mainshock (Fig. 7c). As this mechanism mainly involved fluid-pressure readjustment, with limited fluid flow, it does not imply a seismic migration with depth, which indeed was not observed in the 2014 aftershocks. Later on, in the shallow clusters, fluids flow along the reactivated planes leading to seismic migrations consistent with the observations made by De Barros et *al.* (2019) (Fig. 11, Perturbed state). By this mechanism, the pressure decreases and tends to equilibrate with hydrostatic pressure, leading to the decay with time of the reconstructed pressure. Globally, the very high rate of aftershocks observed during this sequence may be explained by the release of overpressure by the mainshock on top of the coseismic stress transfer.

During a swarm sequence, like in 2003-2004, the fluid-pressure does not decrease with time (Fig. 8a) and triggered seismicity for nearly two years. Moreover, seismic migration consistent with fluid

diffusion is observed for swarms. Therefore, a source of fluid that continuously feeds the swarm, such as a reservoir, is likely beneath the swarm. By analogy with the mainshock-aftershock sequence, the reservoir could be a set of fractures and faults in which fluids are initially trapped and pressurized, even if our study does not bring any information on its nature. However, the initial failures that then release the fluids are probably aseismic here, likely because they are at large depth, below the seismogenic depth. Creep compaction associated with an aseismic slip at depth (Leclère *et al.* 2015) might also be a mechanism to pressurize the fluids. In addition to pressure perturbation, fluid is flowing, leading to seismic migration. In this case, the swarm sequence corresponds to the last step of the model we proposed for the mainshock-aftershocks sequence, similarly to the swarm behaviour sequences observed in the shallow clusters in 2014 (Fig. 11, Perturbed State, top). In the 2003-2004 case, a large volume of water is supposed to flow in order to maintain the swarm active for two years with a seismic migration. The volume that triggers this swarm is estimated to be around 1e7 m^3 (Danré *et al.*, 2022b), similarly to e.g. the long duration Cahuilla swarm, which was also interpreted to be driven by natural fluid-injection (Ross and Cochran, 2021). Assuming a reservoir made of a fracture network with a similar size as the seismic swarm, its total volume will be about 32 km^3 (8 km x1 km x4 km; Daniel et al., 2011). Therefore, the fluid volume (1e7 m^3) required to induce this swarms may be reached by an equivalent porosity decrease of only 0.03%. Such a value seems reasonable considering the porosity of a fractured fault zone that may act as reservoir (Géraud, Diraison and Orellana, 2006; Jeppson, Bradbury and Evans, 2010; Jeanne *et al.*, 2012). However, this process also needs to be combined with the shear-stress transfer. Indeed, as mentioned by Daniel et *al.* (2011), the earthquake-earthquake interaction triggered 59% of the seismicity for the 2003-2004 swarm, and the 41% remaining then might be associated with the fluid-pressure processes. This model may also explain the 1977-1978 swarm (Fréchet and Pavoni, 1979) and the 1989 swarm (Guyoton et al. 1990) that occurred in the Serenne area, indicating similar processes in this area.

In the Serenne area, fluid-overpressure is found increasing with depth, as does the hydrostatic pressure. Therefore, it is likely that the pressurization occurred at different depths within the faults. In our model, the seismic behaviours observed there can be similar to mainshock-aftershocks sequence, where the mainshock is triggered by fluids and breaks barriers to allow pressure to diffuse upward. The pressure might then trigger the aftershock seismicity, similarly to the 2014 mainshock process. Moreover, in the Serenne area, the seismicity is more diffuse than in the Ubaye Valley. It might mean that 1) the fluids might be locally pressurized within the faults at different depths, 2) there is no fluid-pressure feeding system at depth that can trigger large swarms, and 3) fault areas that can be pressurized are of smaller size or disconnected. Therefore, the main differences between these two zones may be related to its fault architecture, and particularly to its hydraulic barriers. Finally, the differences in behaviour between Ubaye Valley and Serenne area might be also impacted by the differences in the lithology composition and by the presence of the Ubaye nappes. In particular, the latter, by acting as a shallow cap-rock, may lead to a slow decay pressure perturbation, hence to much longer seismic sequences in the Ubaye Valley.

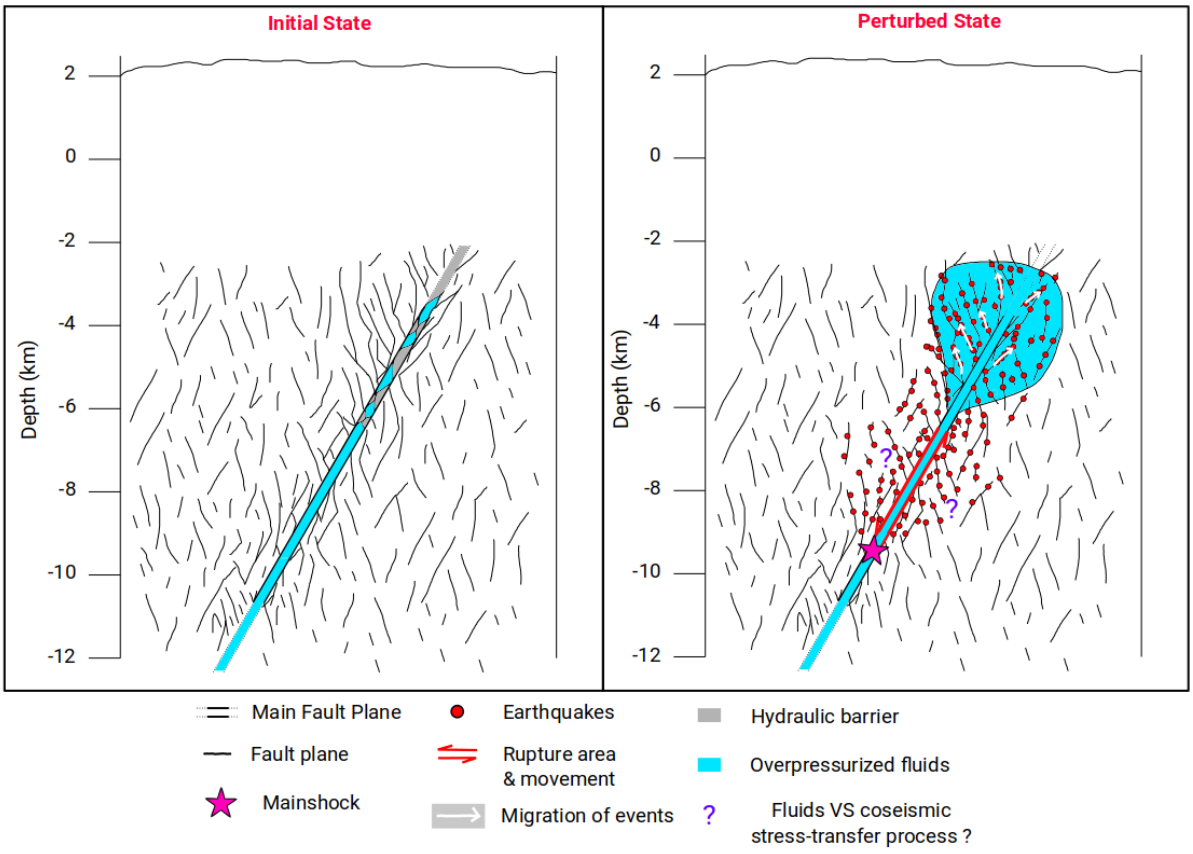

875

876 Figure 11: Conceptual model to explain the different behaviours of the seismicity in the Ubaye Valley.
877 Left, initial state without medium perturbations other than tectonic loading. Right, perturbed state
878 showing mainshock-aftershocks behaviour (bottom) and swarm behaviour (top).

879

880

881

882 # 7. Conclusion

883 Based on the reconstructed focal mechanisms, we determined the stress-state and estimated the
884 overpressures required to trigger earthquakes in the Ubaye Region. We refined this analysis by
885 focusing on specific areas and periods of seismic activity. For the Ubaye Valley, the average stress
886 component orientations are N24°E, 41° for σ1, N201°E, 49° for σ2, and N293°E, sub-horizontal for σ3.

Similar values were obtained for the Serenne area, with some differences in the plunge of σ1 and σ2, which may be due to topographic effects.

We found that most of the events (77%) are triggered by fluids, with a median overpressure of 22%. Overall, the majority of the events (65%), for all sub-areas and periods, required between ~17% and ~40% (~15 MPa and ~40 MPa) of overpressure, which is similar to other natural or induced swarms. Even the events with the largest magnitude seem to be triggered by fluid-overpressure. Therefore, mainshock-aftershocks sequences and swarms are both likely triggered by fluids. The difference in behaviours do not seem to be linked to the overpressure values, but to its time evolution. While overpressure decays with time in an aftershock sequence, it stays at a high level for swarms. Hence, different origin of fluid-pressure may be at play. For the mainshock-aftershock sequences, we proposed that the main faults get pressurized, which trigger the first, largest earthquake. Seismicity is generated on shallower structures through fault-valve behaviour and stress balance. This model is in accordance with the observations made by De Barros et *al.* (2019). On the contrary, swarms need a constant feeding of pressure from a deeper reservoir, likely below the seismogenic depth. Therefore, we here highlighted the role of fluid in both types of earthquake sequences.

Acknowledgements

Some of the figures were made using GMT (Wessel *et al.* 2019), and the colour scales used in the different figures come from the Scientific Colour Map of Crameri (2018). The focal mechanism catalogues are taken from the supplementary materials of Thouvenot et *al.* (2016), Mathey et *al.* (2021a), and Mazzotti et *al.* (2021).

M. Baques would like to thank IRSN and CEA for her funding grants. We would also like to thank Henri Leclère, which provides the focal mechanisms catalogue for the 2003-2004 swarm. We also

thank the CEA, which provides us the LDG catalogue for the 1965-2020 period in the studied area. We thank the editors, two anonymous reviewers and F. Thouvenot for their thoughtful comments that have helped to improve the manuscript.

Data Availability

Seismic data used for the focal mechanisms of the 2014 aftershocks are available online through the RESIF portal (http://seismology.resif.fr/), with permanent stations on https://doi.org/10.15778/RESIF.FR and temporary ones on https://doi.org/10.15778/RESIF.XG2014 and through the INGV portal (http://terremoti.ingv.it/), with permanent stations on https://doi.org/10.13127/SD/X0FXNH7QFY. The resulting focal mechanisms catalogues, the stress-states, the fluid-pressure values, and the codes developed during this paper are available in request. The LDG catalogue (http://www-dase.cea.fr) used in this study is provided in the supplementary materials.

Supporting information

Supplementary figures and data:

Supplementary_materials.docx

LDG_catalogue.txt

References

Amezawa, Y., Maeda, T., Kosuga, M., 2021. Migration diffusivity as a controlling factor in the duration of earthquake swarms. Earth, Planets and Space 73, 1–11.

Baietto, A., Perello, P., Cadoppi, P., Martinotti, G., 2009. Alpine tectonic evolution and thermal water circulations of the Argentera Massif (South-Western Alps). Swiss Journal of Geosciences 102, 223–245.

936 Baisch, S., Rothert, E., Stang, H., Vörös, R., Koch, C., McMahon, A., 2015. Continued geothermal
937 reservoir stimulation experiments in the Cooper Basin (Australia). Bulletin of the Seismological
938 Society of America 105, 198–209.

939 Baisch, S., Vörös, R., Rothert, E., Stang, H., Jung, R., Schellschmidt, R., 2010. A numerical model for
940 fluid injection induced seismicity at Soultz-sous-Forêts. International Journal of Rock Mechanics and
941 Mining Sciences 47, 405–413.

942 Baques, M., De Barros, L., Duverger, C., Jomard, H., Godano, M., Courboulex, F., Larroque, C., 2021.
943 Seismic activity in the Ubaye Region (French Alps): a specific behaviour highlighted by mainshocks
944 and swarm sequences. Comptes Rendus. Géoscience 353, 1–25. https://doi.org/10.5802/crgeos.76

945 Bertil, D., Mercury, N., Doubre, C., Lemoine, A., Van der Woerd, J., 2021. The unexpected Mayotte
946 2018–2020 seismic sequence: a reappraisal of the regional seismicity of the Comoros. Comptes
947 Rendus. Géoscience 353, 1–25.

948 Bott, M.H.P., 1959. The mechanics of oblique slip faulting. Geological magazine 96, 109–117.

949 Byerlee, J.D., 1970. The mechanics of stick-slip. Tectonophysics 9, 475–486.

950 Chiaraluce, L., Ellsworth, W.L., Chiarabba, C., Cocco, M., 2003. Imaging the complexity of an active
951 normal fault system: The 1997 Colfiorito (central Italy) case study. Journal of Geophysical Research:
952 Solid Earth 108.

953 Collettini, C., Trippetta, F., 2007. A slip tendency analysis to test mechanical and structural control on
954 aftershock rupture planes. Earth and Planetary Science Letters 255, 402–413.

955 Courboulex, F., Dujardin, A., Vallee, M., Delouis, B., Sira, C., Deschamps, A., Honore, L., Thouvenot, F.,
956 2013. High-Frequency Directivity Effect for an Mw 4.1 Earthquake, Widely Felt by the Population in
957 Southeastern France. Bulletin of the Seismological Society of America 103, 3347–3353.
958 https://doi.org/10.1785/0120130073

959 Cox, S.F., 2016. Injection-driven swarm seismicity and permeability enhancement: Implications for
960 the dynamics of hydrothermal ore systems in high fluid-flux, overpressured faulting regimes—An
961 invited paper. Economic Geology 111, 559–587.

962 Crameri, F., 2018. Scientific colour maps. Zenodo. https://doi.org/10.5281/zenodo.1243862

963 Daniel, G., Prono, E., Renard, F., Thouvenot, F., Hainzl, S., Marsan, D., Helmstetter, A., Traversa, P.,
964 Got, J.-L., Jenatton, L., 2011. Changes in effective stress during the 2003–2004 Ubaye seismic swarm,
965 France. Journal of Geophysical Research: Solid Earth 116.

966 Danré, P., De Barros, L., Cappa, F., 2022. Inferring fluid volume during earthquake swarms using
967 seismic catalogs. Geophysical Journal International.

968 De Barros, L., Baques, M., Godano, M., Helmstetter, A., Deschamps, A., Larroque, C., Courboulex, F.,
969 2019. Fluid-Induced Swarms and Coseismic Stress Transfer: A Dual Process Highlighted in the
970 Aftershock Sequence of the 7 April 2014 Earthquake (Ml 4.8, Ubaye, France). Journal of Geophysical
971 Research: Solid Earth 124, 3918–3932.

972 De Barros, L., Cappa, F., Deschamps, A., Dublanchet, P., 2020. Imbricated Aseismic Slip and Fluid
973 Diffusion Drive a Seismic Swarm in the Corinth Gulf, Greece. Geophysical Research Letters 47,
974 e2020GL087142.

975 Duboeuf, L., De Barros, L., Kakurina, M., Guglielmi, Y., Cappa, F., Valley, B., 2021. Aseismic
976 deformations perturb the stress state and trigger induced seismicity during injection experiments.
977 Geophysical Journal International 224, 1464–1475.

978 Dumont, T., Schwartz, S., Guillot, S., Malusa, M., Jouvent, M., Monié, P., Verly, A., 2022. Cross-
979 propagation of the western Alpine orogen from early to late deformation stages: Evidence from the
980 Internal Zones and implications for restoration. Earth-Science Reviews 104106.

981 Duverger, C., Godano, M., Bernard, P., Lyon-Caen, H., Lambotte, S., 2015. The 2003–2004 seismic
982 swarm in the western Corinth rift: Evidence for a multiscale pore pressure diffusion process along a
983 permeable fault system. Geophysical Research Letters 42, 7374–7382.

984 Duverger, C., Lambotte, S., Bernard, P., Lyon-Caen, H., Deschamps, A., Nercessian, A., 2018. Dynamics
985 of microseismicity and its relationship with the active structures in the western Corinth Rift (Greece).
986 Geophysical Journal International 215, 196–221.

987 Duverger, C., Mazet-Roux, G., Bollinger, L., Guilhem Trilla, A., Vallage, A., Hernandez, B., Cansi, Y.,
988 2021. A decade of seismicity in metropolitan France (2010-2019): the CEA/LDG methodologies and
989 observations. BSGF - Earth Sciences Bulletin 192.

990 Eyre, T.S., Zecevic, M., Salvage, R.O., Eaton, D.W., 2020. A long-lived swarm of hydraulic fracturing-
991 induced seismicity provides evidence for aseismic slip. Bulletin of the Seismological Society of
992 America 110, 2205–2215.

993 Farrell, J., Smith, R.B., Taira, T., Chang, W.-L., Puskas, C.M., 2010. Dynamics and rapid migration of
994 the energetic 2008–2009 Yellowstone Lake earthquake swarm. Geophysical Research Letters 37.

995 Fischer, T., Horálek, J., Hrubcová, P., Vavryčuk, V., Bräuer, K., Kämpf, H., 2014. Intra-continental
996 earthquake swarms in West-Bohemia and Vogtland: a review. Tectonophysics 611, 1–27.

997 Fojtíková, L., Vavryčuk, V., 2018. Tectonic stress regime in the 2003–2004 and 2012–2015 earthquake
998 swarms in the Ubaye Valley, French Alps. Pure and Applied Geophysics 175, 1997–2008.

999 Fréchet, J., Pavoni, N., 1979. Etude de la sismicité de la zone Briançonnaise entre Pelvoux et
1000 Argentera (Alpes Occidentales) à l'aide d'un réseau de stations portables. Eclogae Geologicae
1001 Helvetiae 72, 763–779.

1002 Gephart, J.W., Forsyth, D.W., 1984. An improved method for determining the regional stress tensor
1003 using earthquake focal mechanism data: application to the San Fernando earthquake sequence.
1004 Journal of Geophysical Research: Solid Earth 89, 9305–9320.

1005 Géraud, Y., Diraison, M., Orellana, N., 2006. Fault zone geometry of a mature active normal fault: A
1006 potential high permeability channel (Pirgaki fault, Corinth rift, Greece). Tectonophysics 426, 61–76.

1007 Godano, M., 2009. Etude théorique sur le calcul des mécanismes au foyer dans un réservoir et
1008 application à la sismicité de la saline de Vauvert (Gard) (PhD Thesis). Université Nice Sophia Antipolis.

1009 Godano, M., Deschamps, A., Lambotte, S., Lyon-Caen, H., Bernard, P., Pacchiani, F., 2014. Focal
1010 mechanisms of earthquake multiplets in the western part of the Corinth Rift (Greece): influence of
1011 the velocity model and constraints on the geometry of the active faults. Geophysical Journal
1012 International 197, 1660–1680.

1013 Goebel, T.H.W., Hosseini, S.M., Cappa, F., Hauksson, E., Ampuero, J.P., Aminzadeh, F., Saleeby, J.B.,
1014 2016. Wastewater disposal and earthquake swarm activity at the southern end of the Central Valley,
1015 California. Geophysical Research Letters 43, 1092–1099.

1016 Gratier, J.-P., Ménard, G., Arpin, R., 1989. Strain-displacement compatibility and restoration of the
1017 Chaînes Subalpines of the western Alps. Geological Society, London, Special Publications 45, 65–81.

1018 Gunatilake, T., 2023. Dynamics between earthquakes, volcanic eruptions, and geothermal energy
1019 exploitation in Japan. Scientific Reports 13, 4625.

1020 Gunatilake, T., Heinze, T., Miller, S.A., Kemna, A., 2021. Hydraulically conductive fault zone
1021 responsible for monsoon triggered earthquakes in Talala, India. Tectonophysics 820, 229117.

1022 Gunatilake, T., Miller, S.A., 2022. Spatio-temporal complexity of aftershocks in the Apennines
1023 controlled by permeability dynamics and decarbonization. Journal of Geophysical Research: Solid
1024 Earth 127, e2022JB024154.

1025 Guyoton, F., Fréchet, J., Thouvenot, F., 1990. La crise sismique de Janvier 1989 en Haute-Ubaye
1026 (Alpes-de-Haute-Provence, France): étude fine de la sismicité par le nouveau réseau SISMALP.
1027 Comptes rendus de l'Académie des sciences. Série 2, Mécanique, Physique, Chimie, Sciences de
1028 l'univers, Sciences de la Terre 311, 985–991.

1029 Hainzl, S., Fischer, T., Čermáková, H., Bachura, M., Vlček, J., 2016. Aftershocks triggered by fluid
1030 intrusion: Evidence for the aftershock sequence occurred 2014 in West Bohemia/Vogtland. Journal of
1031 Geophysical Research: Solid Earth 121, 2575–2590.

1032 Hainzl, S., Fischer, T., Dahm, T., 2012. Seismicity-based estimation of the driving fluid pressure in the
1033 case of swarm activity in Western Bohemia. Geophysical Journal International 191, 271–281.

1034 Hainzl, S., Kraft, T., Wassermann, J., Igel, H., Schmedes, E., 2006. Evidence for rainfall-triggered
1035 earthquake activity. Geophysical Research Letters 33.

1036 Hardebeck, J.L., Michael, A.J., 2006. Damped regional-scale stress inversions: Methodology and
1037 examples for southern California and the Coalinga aftershock sequence. Journal of Geophysical
1038 Research: Solid Earth 111.

1039 Heap, M.J., Faulkner, D.R., Meredith, P.G., Vinciguerra, S., 2010. Elastic moduli evolution and
1040 accompanying stress changes with increasing crack damage: implications for stress changes around
1041 fault zones and volcanoes during deformation. Geophysical Journal International 183, 225–236.

1042 Heinze, T., Hamidi, S., Galvan, B., Miller, S.A., 2017. Numerical simulation of the 2008 West-
1043 Bohemian earthquake swarm. Tectonophysics 694, 436–443.

1044 INGV Seismological Data Centre, 2006. Rete Sismica Nazionale (RSN). Istituto Nazionale di Geofisica e
1045 Vulcanologia (INGV), Italy. https://doi.org/10.13127/SD/X0FXNH7QFY

1046 Jakoubková, H., Horálek, J., Fischer, T., 2018. 2014 mainshock-aftershock activity versus earthquake
1047 swarms in West Bohemia, Czech Republic. Pure and Applied Geophysics 175, 109–131.

1048 Jansen, G., Ruhl, C.J., Miller, S.A., 2019. Fluid Pressure-Triggered Foreshock Sequence of the 2008
1049 Mogul Earthquake Sequence: Insights From Stress Inversion and Numerical Modeling. Journal of
1050 Geophysical Research: Solid Earth 124, 3744–3765.

Jeanne, P., Guglielmi, Y., Lamarche, J., Cappa, F., Marié, L., 2012. Architectural characteristics and petrophysical properties evolution of a strike-slip fault zone in a fractured porous carbonate reservoir. Journal of Structural Geology 44, 93–109.

Jenatton, L., Guiguet, R., Thouvenot, F., Daix, N., 2007. The 16,000-event 2003–2004 earthquake swarm in Ubaye (French Alps). Journal of Geophysical Research: Solid Earth 112.

Jeppson, T.N., Bradbury, K.K., Evans, J.P., 2010. Geophysical properties within the San Andreas Fault Zone at the San Andreas Fault Observatory at Depth and their relationships to rock properties and fault zone structure. Journal of Geophysical Research: Solid Earth 115.

Kakurina, M., Guglielmi, Y., Nussbaum, C., Valley, B., 2019. Slip perturbation during fault reactivation by a fluid injection. Tectonophysics 757, 140–152.

Kanamori, H., Anderson, D.L., 1975. Theoretical basis of some empirical relations in seismology. Bulletin of the seismological society of America 65, 1073–1095.

Kato, A., Saiga, A., Takeda, T., Iwasaki, T., Matsuzawa, T., 2014. Non-volcanic seismic swarm and fluid transportation driven by subduction of the Philippine Sea slab beneath the Kii Peninsula, Japan. Earth, Planets and Space 66, 86.

Kaviris, G., Elias, P., Kapetanidis, V., Serpetsidaki, A., Karakonstantis, A., Plicka, V., De Barros, L., Sokos, E., Kassaras, I., Sakkas, V., 2021. The Western Gulf of Corinth (Greece) 2020–2021 seismic crisis and cascading events: First results from the Corinth Rift Laboratory network. The Seismic Record 1, 85–95.

Kerckhove, C., 1969. La 'zone du Flysch'dans les nappes de l'Embrunais-Ubaye (Alpes occidentales). Géologie alpine 45, 5–204.

Kerckhove, C., Cochonat, P., Debelmas, J., 1978. Tectonique du soubassement parautochtone des nappes de l'Embrunais-Ubaye sur leur bordure occidentale, du Drac au Verdon. Géologie Alpine, Grenoble 54, 67–82.

Kurz, J.H., Jahr, T., Jentzsch, G., 2004. Earthquake swarm examples and a look at the generation mechanism of the Vogtland/Western Bohemia earthquake swarms. Physics of the Earth and Planetary Interiors 142, 75–88.

Larroque, C., Baize, S., Albaric, J., Jomard, H., Trévisan, J., Godano, M., Cushing, M., Deschamps, A., Sue, C., Delouis, B., 2021. Seismotectonics of southeast France: from the Jura mountains to Corsica. Comptes Rendus. Géoscience 353, 1–47.

Le Goff, B., Bertil, D., Lemoine, A., Terrier, M., 2009. Systèmes de failles de Serenne et de la Haute Durance (Hautes-Alpes): évaluation de l'aléa sismique. Rapport BRGM RP-57659-FR 84.

Leclère, H., Cappa, F., Faulkner, D., Fabbri, O., Armitage, P., Blake, O., 2015. Development and maintenance of fluid overpressures in crustal fault zones by elastic compaction and implications for earthquake swarms. Journal of Geophysical Research: Solid Earth 120, 4450–4473. https://doi.org/10.1002/2014JB011759

Leclère, H., Daniel, G., Fabbri, O., Cappa, F., Thouvenot, F., 2013. Tracking fluid pressure buildup from focal mechanisms during the 2003–2004 Ubaye seismic swarm, France. Journal of Geophysical Research: Solid Earth 118, 4461–4476.

1090 Leclère, H., Fabbri, O., Daniel, G., Cappa, F., 2012. Reactivation of a strike-slip fault by fluid
1091 overpressuring in the southwestern French-Italian Alps. Geophysical Journal International 189, 29–
1092 37.

1093 Lohman, R.B., McGuire, J.J., 2007. Earthquake swarms driven by aseismic creep in the Salton Trough,
1094 California. Journal of Geophysical Research: Solid Earth 112.

1095 Ma, S., Eaton, D.W., 2009. Anatomy of a small earthquake swarm in southern Ontario, Canada.
1096 Seismological Research Letters 80, 214–223.

1097 Martínez-Garzón, P., Kwiatek, G., Bohnhoff, M., Dresen, G., 2016. Impact of fluid injection on fracture
1098 reactivation at The Geysers geothermal field. Journal of Geophysical Research: Solid Earth 121, 7432–
1099 7449.

1100 Martínez-Garzón, P., Kwiatek, G., Ickrath, M., Bohnhoff, M., 2014. MSATSI: A MATLAB package for
1101 stress inversion combining solid classic methodology, a new simplified user-handling, and a
1102 visualization tool. Seismological Research Letters 85, 896–904.

1103 Mathey, M., Doin, M.-P., André, P., Walpersdorf, A., Baize, S., Sue, C., 2021a. Spatial Heterogeneity of
1104 Uplift Pattern in the Western European Alps Revealed by InSAR Time-Series Analysis. Geophysical
1105 Research Letters e2021GL095744.

1106 Mathey, M., Sue, C., Pagani, C., Baize, S., Walpersdorf, A., Bodin, T., Husson, L., Hannouz, E., Potin, B.,
1107 2021b. Present-day geodynamics of the Western Alps: new insights from earthquake mechanisms.
1108 Solid Earth 12, 1661–1681.

1109 Mathey, M., Walpersdorf, A., Sue, C., Baize, S., Deprez, A., 2020. Seismogenic potential of the High
1110 Durance Fault constrained by 20 yr of GNSS measurements in the Western European Alps.
1111 Geophysical Journal International 222, 2136–2146.

1112 Mattila, J., 2015. Genesis and evolution of brittle structures in Southwestern Finland and Western
1113 South Africa. Turun yliopisto, Maantieteen ja geologian osasto, Turku. 110s.

1114 Mazzotti, S., Aubagnac, C., Bollinger, L., Coca Oscanoa, K., Delouis, B., Do Paco, D., Doubre, C.,
1115 Godano, M., Jomard, H., Larroque, C., Laurendeau, A., Masson, F., Sylvander, M., Trilla, A., 2021.
1116 FMHex20: An earthquake focal mechanism database for seismotectonic analyses in metropolitan
1117 France and bordering regions. Bulletin de la Société Géologique de France 192.
1118 https://doi.org/10.1051/bsgf/2020049

1119 Michael, A.J., 1984. Determination of stress from slip data: faults and folds. Journal of Geophysical
1120 Research: Solid Earth 89, 11517–11526.

1121 Miller, S.A., Collettini, C., Chiaraluce, L., Cocco, M., Barchi, M., Kaus, B.J., 2004. Aftershocks driven by
1122 a high-pressure CO2 source at depth. Nature 427, 724–727.

1123 Nishikawa, T., Ide, S., 2017. Detection of earthquake swarms at subduction zones globally: Insights
1124 into tectonic controls on swarm activity. Journal of Geophysical Research: Solid Earth 122, 5325–
1125 5343.

1126 Parotidis, M., Shapiro, S.A., 2004. A statistical model for the seismicity rate of fluid-injection-induced
1127 earthquakes. Geophysical Research Letters 31.

1128 Perello, P., Marini, L., Martinotti, G., Hunziker, J.C., 2001. The thermal circuits of the Argentera Massif
1129 (western Alps, Italy): an example of low-enthalpy geothermal resources controlled by Neogene alpine
1130 tectonics. Eclogae Geologicae Helvetiae 94, 75–94.

1131 RESIF, 1995. RESIF-RLBP French Broad-band network, RESIF-RAP strong motion network and other
1132 seismic stations in metropolitan France. RESIF - Réseau Sismologique et géodésique Français.
1133 https://doi.org/doi:10.15778/resif.fr'.

1134 Ross, Z.E., Cochran, E.S., 2021. Evidence for latent crustal fluid injection transients in Southern
1135 California from long-duration earthquake swarms. Geophysical Research Letters e2021GL092465.

1136 Ross, Z.E., Cochran, E.S., Trugman, D.T., Smith, J.D., 2020. 3D fault architecture controls the
1137 dynamism of earthquake swarms. Science 368, 1357–1361.

1138 Ruhl, C.J., Abercrombie, R.E., Smith, K.D., Zaliapin, I., 2016. Complex spatiotemporal evolution of the
1139 2008 Mw 4.9 Mogul earthquake swarm (Reno, Nevada): Interplay of fluid and faulting. Journal of
1140 Geophysical Research: Solid Earth 121, 8196–8216.

1141 Sanchez, G., Rolland, Y., Schreiber, D., Giannerini, G., Corsini, M., Lardeaux, J.-M., 2010. The active
1142 fault system of SW Alps. Journal of Geodynamics 49, 296–302.

1143 Schoenball, M., Dorbath, L., Gaucher, E., Wellmann, J.F., Kohl, T., 2014. Change of stress regime
1144 during geothermal reservoir stimulation. Geophysical Research Letters 41, 1163–1170.

1145 Schultz, R., Skoumal, R.J., Brudzinski, M.R., Eaton, D., Baptie, B., Ellsworth, W., 2020. Hydraulic
1146 fracturing-induced seismicity. Reviews of Geophysics 58, e2019RG000695.

1147 Shapiro, S.A., Huenges, E., Borm, G., 1997. Estimating the crust permeability from fluid-injection-
1148 induced seismic emission at the KTB site. Geophysical Journal International 131, F15–F18.

1149 Shapiro, S.A., Rothert, E., Rath, V., Rindschwentner, J., 2002. Characterization of fluid transport
1150 properties of reservoirs using induced microseismicity. Geophysics 67, 212–220.

1151 Shelly, D.R., Hill, D.P., 2011. Migrating swarms of brittle-failure earthquakes in the lower crust
1152 beneath Mammoth Mountain, California. Geophysical Research Letters 38.

1153 Shelly, D.R., Moran, S.C., Thelen, W.A., 2013. Evidence for fluid-triggered slip in the 2009 Mount
1154 Rainier, Washington earthquake swarm. Geophysical Research Letters 40, 1506–1512.

1155 Shelly, D.R., Taira, T., Prejean, S.G., Hill, D.P., Dreger, D.S., 2015. Fluid-faulting interactions: Fracture-
1156 mesh and fault-valve behavior in the February 2014 Mammoth Mountain, California, earthquake
1157 swarm. Geophysical Research Letters 42, 5803–5812.

1158 Sibson, R.H., 1990. Rupture nucleation on unfavorably oriented faults. Bulletin of the Seismological
1159 Society of America 80, 1580–1604.

1160 Sira, C., Schlupp, A., Schaming, M., Granet, M., 2012. Séisme de Barcelonnette du 26 Février 2012.
1161 Rapport du BCSF 43p.

1162 Sira, C., Schulupp, A., Schaming, M., Chesnais, C., Cornou, C., Deschamps, A., Delavaud, E., Maufroy,
1163 E., 2014. Séisme de Barcelonnette du 7 avril 2014. Rapport du BCSF.

Son, M., Cho, C.S., Choi, J.-H., Jeon, J.-S., Park, Y.K., 2021. Spatiotemporal patterns of the 2020 Haenam earthquake sequence, South Korea: lineament and migration implying fluid-driven earthquake swarm. Geosciences Journal 25, 19–31.

Stein, R.S., 1999. The role of stress transfer in earthquake occurrence. Nature 402, 605–609.

Sue, C., 1998. Dynamique actuelle et récente des Alpes occidentales internes: Approche structurale et sismologique (PhD Thesis). Grenoble 1.

Sue, C., Delacou, B., Champagnac, J.-D., Allanic, C., Tricart, P., Burkhard, M., 2007. Extensional neotectonics around the bend of the Western/Central Alps: an overview. International Journal of Earth Sciences 96, 1101–1129.

Sue, C., Tricart, P., 2003. Neogene to ongoing normal faulting in the inner western Alps: a major evolution of the late alpine tectonics. Tectonics 22.

Talwani, P., Chen, L., Gahalaut, K., 2007. Seismogenic permeability, ks. Journal of Geophysical Research: Solid Earth 112.

Terakawa, T., Miller, S.A., Deichmann, N., 2012. High fluid pressure and triggered earthquakes in the enhanced geothermal system in Basel, Switzerland. Journal of Geophysical Research: Solid Earth 117.

Terakawa, T., Zoporowski, A., Galvan, B., Miller, S.A., 2010. High-pressure fluid at hypocentral depths in the L'Aquila region inferred from earthquake focal mechanisms. Geology 38, 995–998.

Thouvenot, F., Jenatton, L., Scafidi, D., Turino, C., Potin, B., Ferretti, G., 2016. Encore Ubaye: Earthquake Swarms, Foreshocks, and Aftershocks in the Southern French Alps. Bulletin of the Seismological Society of America 106, 2244–2257.

Tricart, P., 2004. From extension to transpression during the final exhumation of the Pelvoux and Argentera massifs, Western Alps. Eclogae Geologicae Helvetiae 97, 429–439.

Tricart, P., Schwartz, S., 2006. A north-south section across the Queyras Schistes lustrés (Piedmont zone, western Alps): Syn-collision refolding of a subduction wedge. Eclogae Geologicae Helvetiae 99, 429–442.

University of Genoa., 1967. Regional Seismic Network of North Western Italy [Data set]. International Federation of Digital Seismograph Networks. https://doi.org/10.7914/SN/GU

Utsu, T., 1961. A statistical study on the occurrence of aftershocks. Geophys. Mag. 30, 521–605.

Utsu, T., Ogata, Y., 1995. The centenary of the Omori formula for a decay law of aftershock activity. Journal of Physics of the Earth 43, 1–33.

Vallée, M., Nocquet, J.-M., Battaglia, J., Font, Y., Segovia, M., Regnier, M., Mothes, P., Jarrin, P., Cisneros, D., Vaca, S., 2013. Intense interface seismicity triggered by a shallow slow slip event in the Central Ecuador subduction zone. Journal of Geophysical Research: Solid Earth 118, 2965–2981.

Vavryčuk, V., Bouchaala, F., Fischer, T., 2013. High-resolution fault image from accurate locations and focal mechanisms of the 2008 swarm earthquakes in West Bohemia, Czech Republic. Tectonophysics 590, 189–195.

1200 Ventura-Valentin, W., Brudzinski, M.R., 2021. Characterization of swarm and mainshock-aftershock
1201 behavior in Puerto Rico article type: Focus Section—Puerto Rico Seismicity/2020 M6. 4 Earthquake
1202 Sequence. Seismol. Res. Lett.

1203 Wallace, R.E., 1951. Geometry of shearing stress and relation to faulting. The Journal of geology 59,
1204 118–130.

1205 Walpersdorf, A., Pinget, L., Vernant, P., Sue, C., Deprez, A., team, R., 2018. Does long-term GPS in the
1206 Western Alps finally confirm earthquake mechanisms? Tectonics 37, 3721–3737.

1207 Wessel, P., Luis, J.F., Uieda, L., Scharroo, R., Wobbe, F., Smith, W.H., Tian, D., 2019. The generic
1208 mapping tools version 6. Geochemistry, Geophysics, Geosystems 20, 5556–5564.

1209 Wynants-Morel, N., Cappa, F., De Barros, L., Ampuero, J.-P., 2020. Stress perturbation from aseismic
1210 slip drives the seismic front during fluid injection in a permeable fault. Journal of Geophysical
1211 Research: Solid Earth 125, e2019JB019179.

1212 Yoshida, K., Hasegawa, A., Okada, T., 2015. Spatial variation of stress orientations in NE Japan
1213 revealed by dense seismic observations. Tectonophysics 647, 63–72.

1214

1215